1 **Resolving the fine-scale velocity structure of continental hyperextension at the**

2 **Deep Galicia Margin using full-waveform inversion**

3 R. G. Davy[1], J. V. Morgan[2], T. A. Minshull[1], G. Bayrakci[1], J. M. Bull[1], D. Klaeschen[3],

4 T. J. Reston[4], D. S. Sawyer[5], G. Lymer[4], D. Cresswell[4].

5 1. University of Southampton, Southampton, United Kingdom.

6 2. Imperial College London, London, United Kingdom.

7 3. GEOMAR Helmholtz Centre for Ocean Research, Kiel, Germany.

8 4. University of Birmingham, Birmingham, United Kingdom.

9 5. RICE University, Houston, TX, United States of America.

10 **Abbreviated title**: Fine-scale velocity structure at Deep Galicia Margin

11 **Corresponding author**: Richard Davy, R.G.Davy@soton.ac.uk, +44 (0) 7783404703

12 **Summary**

13 Continental hyperextension during magma-poor rifting at the Deep Galicia Margin is

14 characterised by a complex pattern of faulting, thin continental fault blocks, and the

15 serpentinisation, with local exhumation, of mantle peridotites along the S-reflector, interpreted

16 as a detachment surface. In order to understand fully the evolution of these features, it is

17 important to image seismically the structure and to model the velocity structure to the greatest

18 resolution possible. Travel-time tomography models have revealed the long-wavelength

19 velocity structure of this hyperextended domain, but are often insufficient to match accurately

20 the short-wavelength structure observed in reflection seismic imaging. Here we demonstrate

21 the application of two-dimensional (2D) time-domain acoustic full-waveform inversion to deep

22 water seismic data collected at the Deep Galicia Margin, in order to attain a high resolution

velocity model of continental hyperextension. We have used several quality assurance

procedures to assess the velocity model, including comparison of the observed and modelled

waveforms, checkerboard tests, testing of parameter and inversion strategy, and comparison

with the migrated reflection image. Our final model exhibits an increase in the resolution of

subsurface velocities, with particular improvement observed in the westernmost continental

fault blocks, with a clear rotation of the velocity field to match steeply dipping reflectors.

Across the S-reflector there is a sharpening in the velocity contrast, with lower velocities

beneath S indicative of preferential mantle serpentinisation. This study supports the hypothesis

that normal faulting acts to hydrate the upper mantle peridotite, observed as a systematic

decrease in seismic velocities, consistent with increased serpentinisation. Our results confirm

the feasibility of applying the full-waveform inversion method to sparse, deep water crustal

datasets.

1. Introduction

In recent years there has been an increase in the availability of high-density seismic datasets

and a significant increase in the power of computers. These combined factors have enabled a

broadening application of seismic full-waveform inversion (FWI). FWI provides a powerful

extension of popular seismic travel-time tomography methods, with the ability to resolve

subsurface velocity structure to half the seismic wavelength, which can be an order of

magnitude smaller than possible with travel-time tomography for a typical crustal target (Wu

and Toksöz 1987; Williamson 1991; Virieux and Operto 2009). Three-dimensional FWI has

yielded impressive results on marine seismic datasets, producing high resolution velocity

2

47 models which can be used directly for geological interpretation or for the migration of

48 reflection seismic data to produce detailed images (e.g. Sirgue *et al.* 2010; Ratcliffe *et al.* 2011;

49 Warner *et al.* 2013; Mispel *et al.* 2013; Jones *et al.* 2013; Mothi *et al.* 2013). The vast majority

50 of such studies have utilised seismic data recorded on either hydrophone streamers or ocean

51 bottom cables (OBC), in relatively shallow marine environments (water depth < 1,000 m).

52 Both hydrophone streamers and OBC possess a high density of receivers, enabling dense

53 sampling of the subsurface for the FWI process (Warner *et al.* 2013). However, the maximum

54 depth of investigation for these methods is restricted to approximately a third to a sixth of the

55 maximum source-receiver offset, limiting their use for studies of crustal scale targets or those

56 in deep water environments (Warner *et al.* 2010; Morgan *et al.* 2013).

57 These limitations can be overcome in deep water environments by applying FWI to wide-angle

58 seismic datasets recorded by ocean bottom seismometers and hydrophones (OBS/H). A limited

59 number of studies have previously applied FWI to OBS/H datasets. Dessa *et al.* (2004) and

60 Operto *et al.* (2006) presented the first results of frequency-domain FWI applied to OBS data,

61 utilising a 2D deployment of 100 instruments at the Nankai Trough, east of Japan. The velocity

62 structure of compressional tectonic features within the accretionary prism and the down going

63 oceanic crust were resolved, where they had not previously been observed in travel-time

64 tomographic models. Kamei *et al.* (2012) applied frequency-domain FWI to a separate

65 deployment of 54 OBS at the Nankai trough, resolving the fine scale velocity structure of

66 megasplay faulting. Recently, Morgan *et al.* (2016) demonstrated the application of

67 three-dimensional (3D) time-domain FWI on an array of 21 OBS situated across the Endeavour

68 oceanic spreading centre of the Juan de Fuca Ridge, revealing low-velocity zones interpreted

69 to represent a magmatic-hydrothermal reaction zone (Arnoux *et al.* 2017). These studies have

70 made use of relatively dense OBS deployments (~ 1 km spacing), or a 3D seismic shooting

71 configuration, both of which are not always possible in academic experiments. We build on

3

these studies by applying FWI to a comparatively sparse dataset (sparse OBS locations recording frequent seismic shots), in order to demonstrate the feasibility of the technique in areas where only 2D or older datasets are available.

Here we demonstrate the application of acoustic 2D FWI to a sparse wide-angle dataset collected on 19 OBS/H at the Deep Galicia Margin in the North Atlantic, with the aim of resolving the fine-scale velocity structure of continental hyperextension. Continental fault blocks within this hyperextended domain can possess dimensions as small as a few kilometres, beyond the limit of what is resolvable with travel-time tomography, making this an ideal target for FWI (Davy *et al.* 2016). We investigate the robustness of our FWI result by testing several parameters influencing the inversion, including the offsets and time windowing of the input data, and uncertainties in the sediment velocity model. Our result cannot be quality checked using 3D phase plots, and so we utilise alternative quality assurances, including checkerboard tests, waveform comparisons, and correlation with reflection seismic imaging. Given the nature of both the dataset and our crustal target, this application of FWI provides an excellent case study to explore the practical limits of this increasingly popular technique.

2. Background

2.1 Geologic setting

Rifting at the Deep Galicia Margin (Fig. 1A) has resulted in the extreme thinning of the continental crust over distances of 100 – 200km. Unaltered crust landward of the proximal rift margin is ~30 km thick and has been thinned through a complex pattern of faulting to only a few km at the distal limits of the margin (Zelt *et al.* 2003; Reston 2009). Initial extensional deformation is inferred to have occurred as high-angle normal faulting, which formed large fault-bound blocks between 10 and 20 km wide, thinning the crust to between 20 and 30 km thick (Ranero and Pérez-Gussinyé 2010). With continued extension of the margin, these

4

continental fault blocks rotated to low-angles, at which point their bounding faults locked up (Ranero and Pérez-Gussinyé 2010). The faulting mechanism responsible for how continued extension was accommodated still remains controversial. McDermott and Reston (2015) propose that the crust deformed through polyphase faulting, where new preferentially oriented normal faults overprinted existing faults and fault blocks. Ranero and Pérez-Gussinyé (2010) suggest that the continued deformation occurred as a sequential pattern of faulting, where new preferentially oriented normal faults were successively formed through the thinned crust, but did not cut the preceding fault. Both of these proposed mechanisms lead to the extreme thinning of the continental crust.

As the margin extended and thinned at an ultra-slow rate (< 10 mm/yr half spreading rate), it allowed time for the entire crust to cool conductively, resulting in the normally ductile mid- and lower-crust becoming progressively embrittled (Srivastava *et al.* 2000; Pérez-Gussinyé and Reston 2001; Pérez-Gussinyé *et al.* 2003). Once the crustal thicknesses reached < 10 km, the entire crust became brittle and coupled, a phenomenon known as continental hyperextension. A fully embrittled crust enabled normal faults to form through the entire crust, from the seafloor to the underlying mantle (Pérez-Gussinyé and Reston 2001; Pérez-Gussinyé *et al.* 2003; Pérez-Gussinyé 2013). These faults acted as conduits, delivering seawater to the upper mantle and forming a layer of serpentinised mantle, which is an inherently weak material (Pérez-Gussinyé and Reston 2001; Reston *et al.* 2007; Bayrakci *et al.* 2016). With continued extension these faults soled out into the structurally weak layer of mantle serpentinite, forming a large and low angle (< 20^0) detachment fault, known as the S-reflector (Fig. 1C), which also corresponds to the crust-mantle boundary in the distal margin (Reston *et al.* 2007). It has been shown recently that these faults, which sole into the S-reflector, preferentially hydrate the upper mantle which results in varying degrees of mantle serpentinisation, observed as a pattern of high and low P-wave velocities (Bayrakci *et al.* 2016; Davy *et al.* 2016). In the final stages of rifting,

5

121 serpentinised subcontinental mantle was exhumed to the seafloor along the S-reflector, and was

122 also emplaced west of this hyperextended domain, forming a structure known as the Peridotite

123 Ridge (Beslier *et al.* 1993), before the onset of seafloor spreading (Davy *et al.* 2016).

124 Sedimentation of this margin occurs at all stages of the rifting process, giving rise to pre-, syn-

125 and post-rift sedimentary units, which are mentioned throughout our interpretations (Fig. 1D)

126 (Ranero and Pérez-Gussinyé 2010).

127 **2.2 Seismic dataset**

128 This study investigates a 2D subset (3D inline 420) of the Galicia-3D seismic experiment,

129 which was performed at the Deep Galicia Margin, west of Spain (Fig. 1A) between 1 June 2013

130 and 2 August 2013 (Fig. 1B); (see Davy *et al.* (2016) and Dean *et al.* (2015) for further details

131 on the wide-angle and multichannel seismic survey parameters, respectively). Multichannel

132 seismic reflection data were recorded by the RV *Marcus G. Langseth* towing four streamers of

133 ~6 km length, spaced 200 m apart, and at a depth of 15 m. Each streamer had 468 channels

134 spaced at 12.5 m intervals. The seismic source comprised two 3,300 cu. in. air gun arrays,

135 towed at a depth of 9 m and fired alternately every 37.5 m (a shot interval of ~16 s), optimal

136 for high resolution 3D reflection imaging, but sub-optimal for wide-angle studies. Processing

137 of this reflection seismic dataset was performed by Repsol, who produced a 3D pre-stack

138 Kirchhoff time migration. Wide-angle seismic arrivals along this 2D profile were recorded by

139 26 ocean-bottom seismometers and hydrophones (OBS/H) from the UK Ocean Bottom

140 Instrumentation Facility (OBIF) (Minshull *et al.* 2005) and GEOMAR (Fig. 1B). The eastern

141 17 OBS/H were spaced densely at ~1.7 km intervals, with the intention to produce a high

142 resolution 2D velocity models of the geologic structure above and below the S-reflector and

143 form the focus of this study. The western 9 OBS/H, spaced at distances of ~3.4 km, cover the

144 Peridotite Ridge (Fig 1C) and the sedimentary basins on its western and eastern flanks. Two of

145 the 26 OBS/H were not retrieved, while another five instruments returned no usable data.

146 Most of the OBS/H in the Galicia-3D seismic experiment recorded seismic shots with a

147 complete azimuthal coverage, allowing these instruments to be accurately relocated by

148 minimising the travel-time misfit between the observed and calculated direct water wave

149 arrival. However, eight OBH along this line were deployed for a shorter period and only

150 recorded shots from a single seismic profile, limiting their ability to be relocated accurately in

151 the cross-line direction (OBH 79-86). On average each instrument was relocated by 299 m.

3. Full waveform inversion

153 The theory behind FWI and its application to seismic data was first developed in the 1980's by

154 Lailly (1983) and Tarantola (1984). It was shown that finite difference modelling of the

155 wavefield through a starting medium, followed by a localised least-squares inversion,

156 minimising the misfit between observed and modelled wavefield, could be used to recover

157 physical properties of the subsurface (Tarantola 1987). Initial applications of FWI were

158 performed in the time domain, but were limited given the high computational demand of the

159 method (Kolb *et al.* 1986). Three decades later and FWI is still performed based on these

160 underlying principles, with modern codes capable of performing FWI in either the time or

161 frequency domain, in two or three dimensions, approximating either the acoustic or elastic

162 wave equation, and can include the effects of seismic attenuation and anisotropy (e.g., Pratt

163 1999; Brossier *et al.* 2009; Warner *et al.* 2013). It has also been shown that the maximum

164 achievable resolution using these codes is on the order of half the seismic wavelength, making

165 it superior to travel-time tomography (Virieux and Operto 2009). Although FWI can extract

166 any physical property which affects the wave equation, it is most commonly used to determine

167 the compressional velocity structure of the subsurface (e.g. Kapoor *et al.* 2013).

168 FWI requires an accurate starting model (typically derived from reflection or travel-time

169 tomography) capable of reproducing the majority of the observed wavefield to within half a

170 seismic cycle at the lowest inversion frequency, observed seismic data, and a derivation of a

171 source wavelet (Virieux and Operto 2009). Forward modelling of synthetic wavefields through

172 the starting model is achieved by solving the numerical wave equation (either acoustic or

173 elastic) through a method of finite differences (Virieux 1986; Operto *et al.* 2007). Residual data

174 are then calculated as the difference between the synthetic and observed data, and then the

175 residuals are back propagated through the velocity model and subsequently cross-correlated

176 with the synthetic data to determine a model update (Tarantola 1984; Pratt *et al.* 1998; Virieux

177 and Operto 2009). Iteration of this process builds an increasingly resolved velocity model,

178 capable of reproducing the observed wavefield to greater degree. As FWI is a localised

179 inversion method it runs the risk of converging to a local minimum, commonly referred to as

180 cycle-skipping (Bunks *et al.* 1995; Sirgue 2006). Cycle-skipping occurs when seismic arrivals

181 in the synthetic wavefield are more than 180° out of phase with that of the observed wavefield.

182 This results in the inversion process attempting to force a match between the observed and

183 synthetic wavefield which is one or more cycles from the true match. In an effort to mitigate

184 against cycle-skipping, it is common practice to start FWI at long wavelengths (low

185 frequencies), which are easier to match within half a cycle, and systematically incorporate

186 shorter wavelengths (higher frequencies) into the modelling, commonly referred to as

187 multiscale FWI (Bunks *et al.* 1995; Sirgue 2006). A complete description of FWI and the

188 underlying theory can be found in Pratt *et al.* (1998) and the review paper of Virieux and Operto

189 (2009).

190 In this study we perform a 2D time-domain, acoustic, isotropic FWI, using the codes of Warner

191 *et al.* (2013). In this code, synthetic traces are calculated through a starting model using a finite

192 difference method and are subsequently scaled so that their RMS amplitude matches that of

193 their corresponding observed trace. Misfit between the respective synthetic and observed traces

194 is calculated as the sum of squares difference for each time interval, with a misfit functional

8

195 representing the misfit over all traces. As this is a time-domain code, the inversion process

196 matches a finite bandwidth of the observed wavefield, defined by a low-pass filter in which the

197 maximum frequency is progressively increased during the inversion. At each bandwidth the

198 misfit functional was minimised by an iterative gradient-based optimisation, which perturbed

199 an input velocity model in order to match the calculated synthetic and respective observed

200 traces, based on the phase shape and relative amplitude of individual arrivals. The code

201 maintains a deterministic relationship between velocity and density, using Gardner's law below

202 the seafloor (Gardner *et al.* 1974).

203 **3.1 Data pre-processing and derivation of the source wavelet**

204 A mixture of four-component ocean-bottom seismometers and single component ocean-bottom

205 hydrophones were utilised in this study; the FWI was performed on the hydrophone channel

206 which was present for all instruments and yielded the highest signal-to-noise ratio. Spectral

207 analysis of the hydrophone data showed that there is a reasonable signal-to-noise ratio at

208 frequencies down to ~3.0 Hz. As we wanted to match the modelled wavefield to the observed

209 wavefield, without cycle skipping, we included signal at the lowest frequencies possible. A

210 minimum phase Ormsby band-pass filter with corner frequencies of 2.0, 3.0, 4.5 and 6.5 Hz

211 was applied to the hydrophone data in order to isolate the low-frequency signal from unwanted

212 noise (Fig. 2A). Typical data pre-processing for the purpose of FWI may look to maintain the

213 lower frequency data by simply applying a low-pass filter, but we needed also to diminish the

214 effects of coherent low-frequency noise from the previous seismic shot. A top mute was applied

215 ~0.1 s before the first seismic arrival, in order to remove the noisy water column, and a bottom

216 mute was applied 1.8 s after this top mute (Fig. 2B) in order to include the first-arriving

217 wavefield which, at these frequencies, is about 1.0 - 1.5 s in length (Fig. 2A). This muting

218 process creates a time window for the input field data which incorporates the direct water

219 arrival and refractions through the crust (Pg) and upper mantle (Pn) (Fig. 2B).

220   We use a free surface to represent the reflective sea surface, so, we use a deghosted source

221   wavelet to generate synthetic data for FWI. The deghosted source wavelet is obtained using a

222   Weiner matching filter and here, we used the following steps: 1) guessing a source wavelet by

223   selecting a clear noise-free near-offset direct water-wave arrival into an OBS (OBS46 was

224   selected), windowing this arrival by 1 s, and applying an identical bandpass filter to this

225   guessed source wavelet and field data (Ormsby band-pass filter with corner frequencies of

226   2.0,3.0, 4.5and 6.5 H); 2) generating a synthetic water-wave arrival for the selected OBS using

227   the guessed band-pass filtered source wavelet and starting model; 3) finding the inverse filter

228   that matches this synthetic trace to the observed trace; and 4) applying this inverse filter to the

229   initial source guess to generate the new source wavelet. This new source was then used to

230   generate the nearest-offset direct wave through the water for all OBS and compared to the

231   equivalent observed arrival (Fig. 3). The excellent match between the observed and synthetic

232   data shows that this source wavelet is appropriate for all the OBS. The similarity of the

233   waveforms for all OBS indicates that there is no significant change in the source wavelet during

234   the survey, and that there are no significant differences in the OBS response at the frequencies

235   used in the inversion.

236   **3.2 Starting model**

237   The starting model for the FWI process is a modified version of the 2D compressional seismic

238   travel-time tomography model described by Davy *et al.* (2016). This model was developed

239   using OBS data collected from the Galicia-3D seismic experiment, supplemented with data

240   from the ISE-1 seismic profile (Sawyer *et al.* 1997; Zelt *et al.* 2003), and inverted using the

241   "TOMO2D" travel-time inversion code of Korenaga *et al.* (2000). The final TOMO2D model

242   has an overall travel-time misfit of 53 ms, and a chi-squared value of 0.97. We shortened this

243   model to include only the easternmost 68 km of the seismic profile where the OBS are more

244   closely spaced, to a depth of 12 km, and defined the model on a grid with a horizontal and

        10

245 vertical spacing of 50 m. FWI requires 4 - 5 model nodes per seismic wavelength (Warner *et*

246 *al.* 2013), and so with water velocities of ~ 1.5 km s^{-1} a node spacing of 50 m allows inversion

247 frequencies of up to 6.0 -7.5 Hz. In the TOMO2D analysis, a constant velocity of 1.52 km s^{-1}

248 was used for the water column. This is sufficient for travel-time tomography, but not for

249 reproducing consistently the first seismic arrivals to within half a cycle of those observed in

250 the field data. Sound velocity profiles, used for the processing of the multibeam bathymetry

251 collected during the survey, were used in place of this constant velocity approximation. The

252 resulting model gives an accurate fit of the direct arriving waveforms through the water-column

253 (12.7 ms for all instruments, on average), as shown in Fig. 3.

254 Sediment velocities in this starting model were determined by the forward modelling of a

255 prominent sedimentary reflector and very limited sediment refractions, and are therefore

256 relatively unconstrained. This is the result of the large crossover distance between the direct

257 water wave and the refracted arrivals from the subsurface, dictated by the depth of the

258 instrument deployment. The effect of uncertainty in sediment velocities on the final FWI

259 velocity model is examined later in the paper.

260 The velocity model was smoothed in both the horizontal and vertical directions in order to

261 remove any features that have a shorter wavelength than obtainable by FWI at the lowest

262 inversion frequency. A 2D convolution filter, using 3 samples in the vertical direction (150 m)

263 and 9 samples in the horizontal direction (450 m), was used for this smoothing process. Our

264 starting model can be seen in Fig. 4A.

265   **3.3 Data selection**

266 Using this starting velocity model, synthetic receiver gathers were produced with the same

267 source-receiver geometry as the original seismic experiment (Fig. 2C). Synthetic gathers were

268 used as a quality control for the field data to be input into the FWI process. Of the 20

11

269   instruments which yielded useable data, one was rejected for being too noisy. The final

270   instrument coverage used for the FWI is shown in Fig. 1B.

271   Within the offset range between 0 m and 5,000 m the first arrivals comprise direct water waves

272   and sub-horizontally travelling turning waves which sparsely sample the shallow sub seafloor

273   (Fig. 2B). When included in the inversion these arrivals tend to dominate due to their large

274   amplitudes, and the inversion attempts to match changes in waveform structure by introducing

275   rapid changes in shallow sub-seafloor velocities which are poorly constrained. Pg and Pn

276   arrivals travel sub-vertically through the shallow section below each OBS, and therefore pass

277   relatively rapidly through this region, so their travel-times will not be significantly affected by

278   the shallow velocity structure. Thus, it was decided to exclude this offset range (0 – 5000 m)

279   from the inversion, and not attempt to resolve velocity in the shallow sub seafloor, which is a

280   region of low scientific interest.

281   We assessed the data from each individual instrument to identify the maximum offsets to which

282   the first seismic arrival could be positively identified and matched to the synthetic wavefields

283   to within half a seismic cycle. Travel-time picks from Davy *et al.* (2016) were used as guidance

284   in this process. These maximum offsets were then used as the upper bounds for data input for

285   the respective instrument. Maximum input data offsets ranged from 13.0 to 23.0 km across the

286   19 instruments utilised in the inversion (Fig. 2B shows maximum data offsets used for OBS

287   46).

288   **3.4 Inversion**

289   We assumed an isotropic medium for the inversion, based on previous joint reflection and

290   refraction travel-time tomography (Davy *et al.* 2016). These joint inversions resolved the

291   S-reflector by constraining the velocity field using refraction data and determining the reflector

292   depth using wide-angle reflections. These results showed an excellent match to the S-reflector

293   resolved in reflection imaging, where ray-paths are near vertical. This observation indicates

294   that any anisotropy is quite weak, justifying our assumption of isotropy.

295   We developed the inversion by increasing progressively the cut-off frequency of the low pass

296   filter applied to the input data, which was set at 3.0, 3.4, 3.9, 4.5 and 5.2 Hz (Fig. 4). Velocities

297   of below 2.0 km s^{-1} in the starting model were kept constant during the inversion to keep the

298   water velocity and sea bottom fixed, since these parameters had been determined

299   independently, and were confirmed by synthetic direct water waves through the starting model

300   (Fig. 3). Velocities were not allowed to be updated above 8.50 km s^{-1} as this was considered

301   to be the maximum realistic value for the uppermost mantle here. The inversion process was

302   iterated 10 times for each filter setting, with the resulting velocity model acting as the input to

303   the next inversion iteration (Fig. 4). After 10 inversion iterations at each bandwidth the

304   reduction in the model misfit was less than 0.5% of the previous inversion iteration, which we

305   believed to be a sufficient convergence (Fig. 5). Relatively small reductions in the misfit

306   functional were seen for each inversion frequency, see Table 1.

307   The complete inversion process runs through 50 iterations to produce the final inversion model

308   (Fig. 4F). Systematically introducing higher frequencies of input data into the inversion

309   process gradually increases the resolution of the resulting velocity model (Fig. 4A-F).

310   Testing of the inversion parameters included examining the effects of: the maximum data

311   offsets used, the length of the time window around the first seismic arrival, and uncertainty in

312   the sediment velocities in the starting model. The results of these parameter tests were checked

313   against reflection seismic images, and the observed field data, in order to make informed

314   decisions on the best parameterisation. The next three subsections describe the results of these

315   tests.

316

317   **3.5 Data offsets**

318   One of the limitations of this dataset is the range of useable data offsets. Given the deep-water

319   setting, Pg refractions only become first arrivals at offsets of > 5,000 m, reducing our ability

320   to resolve shallow subsurface structure. At longer offsets (> ~12,000 m) the data become

321   adversely affected by coherent noise from the third multiple (and higher order multiples) of the

322   previous seismic shots (Fig. 2A). This is problematic because the crustal targets (fault rotated

323   continental blocks, the S-reflector and uppermost mantle) are up to 5,000 m below the seafloor,

324   but we can only expect to resolve targets at depths approximately between a sixth and third of

325   the maximum source-receiver offset (Warner *et al.* 2010; Morgan *et al.* 2013). This means that

326   our inversion model, for data offsets > 12,000 m, may be prone to noise-induced artefacts when

327   attempting to resolve structure at depths greater than 2,000 – 4,000 m below the seafloor. To

328   test whether our selected maximum data offsets (between 13.0 and 23.0 km) produced a robust

329   model, we tested arbitrary maximum data offsets of 10, 15 and 20 km for all instruments used

330   in the inversion. All other inversion parameters were identical to those described in section 3.4.

331   Fig. 6 shows the resulting models and 1D profiles at set distances through each model.

332   When limiting input data offsets to 10 km (Fig. 6A), the resulting velocity model has many

333   closed velocity contours, high lateral and depth variability, and features which would be

334   described as non-geologic. This is expected given the sparse coverage and relatively shallow

335   depth of penetration when offsets are limited to 5 to 10 km, as waves are expected to only travel

336   to depths of 1.6 – 3.3 km below the seafloor. It can be seen in the 1D plots (Fig. 6E-J) that the

337   model utilising 10 km data offsets has a good correlation with the trends of the other models to

338   depths of ~ 1.2 – 3.0 km below the seafloor, as would be expected. The only exception to this

339   is at ~ 40 km profile distance (Fig. 6H). Below these depths, the 10 km offset model varies

340   from the other models by up to 1.38 km s^{-1} (e.g. 3.0 km below the seafloor at 50 km profile

341   distance), because the model is unconstrained at these depths.

14

342   The remaining three models share common features and velocity values. These models appear

343   much smoother than that produced using data offsets from 5 to 10 km. The 1-D velocity profiles

344   confirm that the models have common trends with depth, throughout the model (Fig. 6E-J), but

345   we observe that the model utilising offsets of 15 km deviates from our final inversion model

346   and that using maximum offsets of 20 km, at depths greater than 4 km below the seafloor on

347   profiles at 10, 30 and 50 km. Again, these deviations are unsurprising given that the expected

348   depth of penetration when using maximum offsets of 15 km is up to 2.5 – 5.0 km.

349   This similarity, especially between models using 15 and 20 km offset of input data, indicates

350   that incorporating data with coherent noise yields results which are comparable to those

351   inversions which exclude noisy data altogether.   These results also suggest that the FWI is

352   relatively insensitive to noise.

353   **3.6 Data windowing**

354   Data input into the inversion process were top and bottom muted, allowing a 1.8 s window of

355   data to be matched in the inversion process. This time window was determined heuristically in

356   order to include only the primary compressional seismic phase arrivals (i.e. Pg and Pn, Fig.

357   2A), while excluding mode-converted later arrivals, which cannot be reproduced by the

358   acoustic wave approximation (Jaiswal *et al.* 2008). Windows of 1.8 s were selected, based on

359   inspection of the length of the band passed first-arriving waveform (Fig. 2A). To investigate

360   the effect of the data window length, the inversion process was run also with data windows of

361   lengths 1.0, 1.5, 2.0 and 2.5 s (Fig. 7). It appears that longer window lengths introduced more

362   complicated structure to the resulting velocity model, a result of the inversion process trying to

363   fit the later parts of the seismic coda and later arrivals. A time window of 2.5 s resulted in a

364   rough model with a significant number of closed velocity contours, which are geologically

365   unlikely for this setting. Conversely, a time window of 1.0 s resulted in a smooth model, which

15

366   is geologically reasonable, but failed to match reflections in the seismic images as well as

367   inversion model using a time window of 1.8 s. We also observed a significant decrease in

368   seismic velocity in the resolved upper mantle in the central section of the profile, with an

369   increasing window length (depths of 9.0 – 10.5 km, 25.0 – 32.0 km profile distance, Fig. 7C-

370   D; deeper than 4.0 km below seafloor in Fig. 7G). Despite these differences, the overall velocity

371   structure observed in the plots and the trends of the 1D velocity profiles, remained relatively

372   constant. Consistency in the resulting FWI models and the observed depth-velocity profiles,

373   when using time windows of 1.0, 1.5 and 2.0 s for FWI, indicates that our chosen time window

374   of 1.8 s is appropriate.

3.7 Sedimentary velocities

376   As mentioned earlier in this section, the post-rift sediment velocities in the starting model were

377   poorly constrained, so we test the effects of varying post-rift sedimentary velocities in the

378   starting model. In the original model, the post-rift sediments were defined by two discrete

379   sedimentary layers; the top has velocities increasing from 2.00 to 2.15 km s^{-1}, while the bottom

380   layer has velocities increasing from 2.30 to 2.60 km s^{-1}. These layers were constrained by inter-

381   sedimentary reflectors (at offsets < 5,000 m) and limited sedimentary refractions (at offsets >

382   5,000 m). To test the uncertainty in sedimentary velocities in our starting model, we performed

383   the TOMO2D travel-time inversion of Davy *et al.* (2016) with starting models possessing low

384   sediment velocities (1.80 – 2.00 km s^{-1}), high sediment velocities (2.60 – 3.00 km s^{-1}), a

385   low-velocity gradient (2.30 – 2.50 km s^{-1}) and a high-velocity gradient (1.80 – 3.20 km s^{-1}). All

386   travel-time inversion parameters remained identical to that described in Davy *et al.* (2016). The

387   outputs of these travel-time inversions were then used as the starting models for the FWI

388   process, with the inversion results observable in Fig. 8. With the exception of the low sediment

389   velocity model, the general velocity structure below the post-rift sediments remains consistent.

390   Where post-rift sediment velocities are low, higher velocities are observed directly below the

16

391   top of the syn-rift sediments, and vice-versa where the post-rift sediment velocities are high.

392   This behaviour is a result of both the travel-time tomography and FWI. The phenomenon is

393   amplified in areas of thicker post-rift sediment (i.e.: at 10, 20 and 50 km profile distance). For

394   example, at 50 km profile distance the difference between the low and high sediment velocity

395   models is 1.75 km s^{-1} at 1.65 km below the base of the post-rift sediment (Fig. 8I). This result

396   indicates that variations in the starting post-rift sedimentary velocities are compensated for by

397   the velocities below the post-rift sediment, in order for the total travel-times to fit. Along the

398   representative depth-velocity profiles (i.e.: 10, 20, 30, 40, 50 and 60 km profile distance), the

399   depth-averaged range of velocities recovered for the range of starting models, excluding the

400   low-velocity post-rift sediment velocity model, is 0.12 km s^{-1}. We conclude that, since the

401   sediments are unlikely to have such low velocities, the overall velocity structure of the

402   inversion models below the post-rift sediment are minimally affected by uncertainty in the

403   postrift sedimentary velocities.

404   **3.8 Assessing the modelled wavefield**

405   One measure of the success of FWI is how accurately the observed wavefield is reproduced,

406   and this is done by comparison with the synthetic wavefield. Fig. 9 shows the propagation of

407   the source wavelet through the final inversion model to produce the synthetic wavefield. In this

408   example, we have reversed the source and receiver configuration and are treating the OBS 46

409   as the seismic source, and the shot locations as receivers. This approach demonstrates the

410   interaction of the wavefield with subsurface structure, and how that results in the observed

411   wavefield. East of OBS 46, the wavefield refracts through significant subsurface topography

412   in the form of a rotated continental fault block, giving the travel-time of the first seismic arrival

413   significant lateral variability (arrow ii, Figure 2C). Conversely, west of OBS 46, the top of the

414   rotated continental fault block dips smoothly westward, resulting in a first seismic arrival of

17

415 little variation (arrow i, Figure 2C). These synthetically produced travel-time features, resulting

416 from the modelled subsurface topography, match those in the observed wavefield (Fig. 2A-B).

417 In order to compare the match between the observed and modelled wavefields, we interleaved

418 traces from alternative offset bins of 200 m (i.e.: traces with instrument offsets between 200 –

419 400 m, 600 – 800 m, etc. are taken from the observed wavefield and are combined with traces

420 with instrument offsets between 0 – 200 m, 400 – 600 m, etc. from the synthetic wavefield)

421 (Figs 10-12A-B). Where the wavefields match, a continuous wavefield will be observed over

422 distances greater than the 200 m trace bins. Where the match is poor, a discontinuous wavefield

423 will be observed over such distances. Comparing the observed wavefield with the synthetic

424 wavefield through the starting model (Figs 10-12A), it can be seen that the direct water arrival

425 (-7.0 – 7.0 km) shows high continuity, indicating that the starting velocity model has reasonably

426 accurate water and sub-seafloor velocities. The wavefield appears to be fairly consistent at

427 some wider offsets, for example between -11 to -15 km on OBS 46 (Fig. 11A) and -10 to -14

428 on OBS 54 (Fig. 12A), indicating that the starting model at depth is close to the true velocity

429 structure in particular areas. There are also notable mismatches in the first seismic arrivals,

430 outside the direct water arrival, for example at offsets between -7 and -11 km and between 7

431 and 13 km on OBS 46 (Fig. 11A) and 6 to 10 km on OBS 37 (Fig. 10A), which indicates that

432 the velocities in sections of the thinned continental crust are not reproducing the wavefield

433 accurately. However, these mismatches appear to be less than half a seismic cycle, which is a

434 prerequisite to avoid cycle skipping during the FWI process. Significant improvements in the

435 match between wavefields are observed when comparing the observed and synthetic wavefield

436 through the FWI velocity model (Figs 10-12B). Areas previously mismatched (for example

437 between offsets of 7 – 13 km on OBS 46) now appear more continuous (see arrows) indicating

438 that the FWI process has modified the subsurface velocities in such a way that the travel-time

439 and phase of these synthetic waveforms match those that are observed. Where the starting

18

440   model already matched the observed wavefield well there is little to no change, as would be

441   expected.

442   Directly comparing traces at set offsets also shows how the synthetic waveforms are modified

443   through the FWI process. Figs 10C-H, 11C-G, and 12C-G, show trace-to-trace comparisons of

444   the observed wavefield and synthetic wavefield through the starting velocity model, while Figs

445   10I-N, 11H-L, and 12H-L, show trace-to-trace comparisons of the observed wavefield and

446   synthetic wavefield through the final velocity model. Despite the small changes in the inversion

447   misfit (Fig. 5), we observe significant improvements in the synthetic wavefield. For example,

448   at offsets of -10.05, -7.52, 8.63 and 11.93 km on OBS 46 (Fig. 10D-G), the synthetic traces

449   through the starting model exhibit shapes close to the observed waveform, but with amplitude

450   differences and phase shifts within half a seismic cycle. After the FWI, the synthetic traces

451   have relative amplitudes and phases that match well the observed traces (Fig. 10J-M),

452   indicating that the new velocity model is a more accurate representation of the subsurface.

453   Observed traces at the furthest input offsets (i.e.: -14.92 and 16.80 km on OBS 46, 18.06 km

454   on OBS 37, and -17.57 km on OBS 54, Figs 11I, 11N, 10L, and 12H, respectively) are being

455   affected by coherent noise, and FWI is struggling to match these more complicated waveforms.

456   It appears that the trace at -14.92 km on OBS 46 is cycle skipped in the starting model, and

457   although the inversion has led to an improvement in the shape of the waveform it has not

458   changed its travel-time, which should be earlier. The onset of reduced performance of FWI at

459   longer offsets reinforces the decision to limit the offsets of the input data, based on visual

460   inspection of the match between the observed data and synthetic data from the starting model.

461   **3.9 Checkerboards**

462   The maximum achievable resolution of the final FWI velocity model was assessed by a series

463   of checkerboard tests (Zelt and Barton 1998). Alternating velocity perturbations of $\pm$ 2% were

19

464   introduced into the starting velocity model in checkerboard patterns to create reference models

465   with anomaly dimensions of 10.0 km x 2.0 km, 5.0 km x 1.0 km, and 2.5 km x 0.5 km (Fig. 13).

466   Small velocity perturbations of $\pm$ 2% are used in order to avoid major changes in the modelled

467   wave-paths, which could lead to the synthetic data generated from the checkerboard and

468   starting model being cycle skipped. Synthetic receiver gathers were then produced through

469   these reference models by forward modelling of the wavefield, using the same shot-receiver

470   geometry as the receiver gathers used in the FWI. These synthetic receiver gathers were

471   windowed and inverted with identical FWI parameters. The differences between these

472   inversion results and the unperturbed starting velocity model were used to determine the length

473   scale of structure resolvable in the final FWI model (Fig. 13).

474   There is an observable diagonal smearing of the resolved checkerboard patterns at the eastern

475   and western limits of the model, for all scales of velocity perturbation. This phenomenon occurs

476   between checks of equal polarity, at profile distances < 10 km and > 50 km. This smearing is

477   likely to be the result of the subsurface being sampled by unidirectional wave propagation and

478   limited data offsets in these areas of the model.

479   Large-scale structure (10.0 km x 2.0 km) is very well resolved throughout the central portion

480   of the model, but exhibits a small deterioration in the recovered anomaly amplitudes below 10

481   km depth. Medium-scale structure (5.0 km x 1.0 km) is still well resolved, but starts to exhibit

482   slight smearing between checks where there is lower instrument coverage (e.g. 5.0 – 30.0 km

483   profile distance), and again at depths > 10 km. Fine-scale structure (2.5 km x 0.5 km) is the

484   least well resolved, as is to be expected, but much of the structure at this scale is still

485   recoverable throughout the model. Fine-scale structure is particularly well resolved between

486   profile distances of 30.0 – 42.0 km and 52.0 – 60.0 km, where the coverage of instruments is

487   densest. Other regions of the model start to reveal a greater degree of smearing between checks,

488   primarily between diagonally linked checks.

        20

489　The results of these resolution tests exhibit a significant improvement over the minimum

490　resolution of approximately 5.0 x 2.5 km, achieved in the travel-time tomography of Davy *et*

491　*al.* (2016). However, it should be noted that these resolution tests are done with synthetically

492　produced wavefields and thus represent the maximum achievable resolution with the given

493　experimental geometry.

494　**4　Results and discussion**

495　The final FWI velocity model in depth can be seen in Figs 4F and 6D. Overall, the long-

496　wavelength velocity structure remains consistent with that of the starting travel-time

497　tomography model. Within the velocity model we observe well-defined rotated continental

498　fault blocks which overlie the S-reflector, and the Peridotite Ridge in the west. The FWI result

499　reveals features in the velocity model with shorter-wavelengths and a greater lateral variability

500　to those that are observed in the starting model, indicating an increase in the resolution of the

501　velocity structure along this seismic line.

502　**4.1 Comparison with seismic images and interpretations**

503　In order to assess whether the FWI has resolved the velocities of fine-scale subsurface structure,

504　we compare the final velocity model with the structure observed in reflection seismic imaging.

505　To make this comparison we have utilised existing high-resolution 3D multichannel reflection

506　seismic images, which have been processed through to 3D pre-stack Kirchhoff time migration.

507　This reflection imaging was produced using the full 3D seismic volume, which has a wide

508　azimuth of shots and receivers, and yields a high-fidelity image of the subsurface. We

509　converted our final FWI velocity model to time, and overlaid it onto the time migrated

510　reflection image of seismic inline 420 (Figs 14 and 15). Additionally we have overlain the

511　interpretation of significant and relevant faults and geological horizons. Significant horizon

512　reflections are seen from the base of the post-rift sediment, a strong intra syn-rift reflector, the

21

513   top of crystalline basement, and the S-reflector. These interpretations have been made

514   consistently throughout the 3D seismic volume and are independent from both our starting and

515   FWI velocity models. For the prominent normal faults and continental blocks observed through

516   this section, we have adopted the naming convention of F3 – F8 and B3 – B7, respectively

517   (Ranero and Pérez-Gussinyé 2010; Borgmeyer 2010) .

518   **4.1.1   Long-wavelength structure**

519   Long-wavelength features that were already present in the starting velocity model show a

520   strong correlation with the large-scale features imaged in the reflection seismic, such as the

521   Peridotite Ridge, the major fault-rotated continental blocks (e.g. B3 – B6) and the S-reflector

522   detachment surface (Fig. 14D) (Davy *et al.* 2016). These features retain their long-wavelength

523   velocity structure through the FWI process, and shorter wavelength velocity features are

524   revealed within the previously resolved features. The most apparent and significant changes to

525   the velocity model occur in continental fault blocks B4-B7 within the pre / syn-rift sediments

526   and the top of crystalline basement. Areas of particular interest are identified by dashed boxes

527   in Fig. 14 and are shown at a larger scale in Fig. 15. Features within these areas are discussed

528   in detail in the next sub-section. Outside of these regions, we observed noticeable features at

529   both the western and eastern limits of the inversion model.

530   There is a deepening of seismic velocities between $6.0 – 7.0$ km s^{-1} on the eastern flank of the

531   Peridotite Ridge (7.0 – 12.0 km profile distance, arrow i, Fig. 14E). This deepening could

532   indicate that the serpentinisation of the mantle peridotite in this area is more pervasive than

533   previous models have indicated. This area of decreased seismic velocities is coincident with

534   the interpreted western limit of the S-reflector and the suggested location of normal fault F8,

535   which could have acted as a conduit, enabling the hydration and serpentinisation of this area.

22

536   At the eastern end of the profile, we observe top basement velocities ($\sim$ 5.5 km s^{-1}) resolved in

537   both blocks B3 and B2, east of their interpreted bounding faults, F4 and F3, respectively

538   (arrows ii and iii, Fig. 14E). The velocity in the up-dip end of the rotated fault blocks increases

539   to values consistent with crystalline basement, indicating that the internal structure of these

540   blocks is resolved to a greater degree. Additionally, there is a shallowing of mantle velocities

541   ($\sim$ 8.0 km s^{-1}) below continental block B2, which removes an apparent step in these velocities

542   observed in the starting model (arrow iv, Fig. 14E).

543   **4.1.2   Continental fault blocks**

544   The starting velocity model has minimal adherence to the interpreted geological horizons

545   within fault block B4 – B7 (Fig. 15D-F). Velocity contours cut across reflection horizons

546   obliquely, where they would be expected to run parallel, and no sharp velocity changes are

547   observed laterally across normal faults. Significant improvements are observed in the FWI

548   velocity model (arrows i-xiii in Fig. 15G-I), relative to the starting model, with an increased

549   correlation between the velocity field and a number of the interpreted faults and reflection

550   horizons. In some areas we also observe increased correlation between the velocity model and

551   seismic reflections, which have not been interpreted previously (dashed lines Fig.15G-I).

552   Particularly good improvement is observed in the internal velocity structure of continental

553   blocks B6 and B7 (arrows i-v, Fig. 15G-H, and to a lesser degree B6a and B5 (arrows vi-x,

554   Fig.15H). In these regions of the model we see a rotation of the velocity field, particularly at

555   the top of crystalline basement, so that velocity contours run parallel to significant reflections.

556   For example, in block B6 (Fig. 15E), starting velocities at the top of the interpreted crystalline

557   basement of $\sim$ 4.55 km s^{-1} on the up dip (western) end, and $\sim$ 5.95 km s^{-1} on the down dip end

558   (eastern). This gives a velocity difference of $\sim$ 1.40 km s^{-1} along a lithological boundary where

559   we would expect to observe a roughly constant velocity. After the inversion the velocities in

560   these same model locations are now $\sim$ 5.35 km s^{-1} and $\sim$ 5.65 km s^{-1}, up dip and down dip,

23

561 respectively; a velocity difference of only ~ 0.30 km s^{-1} along the same boundary. Similar

562 improvements in the crystalline basement velocities are observed in block B7 (Fig. 15D and

563 G), and less substantial improvements are also seen in blocks B6a and B5 (arrows vi and ix,

564 Fig. 15E and H).

565 Despite not resolving constant velocities along the layer boundaries within block B4 (Fig. 15F

566 and I), the FWI process has begun to introduce the appropriate higher velocities (~ 6.00 km s^{-1})

567 into the area interpreted as crystalline basement. These velocities are prominently resolved next

568 to the westward fault, F5 (arrow xii, Fig. 15I). The area of high velocity within the crystalline

569 basement of B4 now exhibits a large velocity contrast laterally across normal fault F5, with the

570 syn-rift unit of block B5 (arrow xi, Fig. 15I). We observe a lateral velocity contrast of

571 ~ 1.70 km s^{-1} over a distance of less than 1.00 km across fault F5, where the starting contrast

572 was previously ~ 0.75 km s^{-1}. This result indicates an increased resolution of the velocity

573 changes across normal faults, which are inferred to have juxtaposed different lithologies against

574 one another. This improvement in the lateral velocity contrast is also observed between the

575 crystalline basement of block B6 and the syn-rift unit of block B7, across fault F7 (arrow ii,

576 Fig. 15G). There is also evidence of a previously unidentified fault within block B6a, between

577 faults F6 and F6a (Fig. 15H). A sharp lateral velocity contrast of ~1.50 km s^{-1} (arrow viii, Fig.

578 15H), and westward dipping velocity field, highlights a weak reflector which we interpret as a

579 normal fault.

580 Even though these areas of the FWI model exhibit apparent improvement, there are areas where

581 we now observe velocity patterns which do not match the reflection image and its

582 interpretation. Within fault block B4 (Fig. 15I) a large portion of the unit interpreted as

583 crystalline basement remains unresolved, with uncharacteristically low velocities. There are

584 also areas where we observe a chaotic pattern in the velocities, exhibiting little correlation to

585 imaged sedimentary reflectors. A similar uncorrelated velocity pattern is observed in the

24

586   sedimentary units of block B5 (Fig. 15H-I). A small, and unlikely, circular velocity inversion

587   is observed directly east of fault F8 (Fig. 15G). These areas all appear to be well resolved in

588   the checkboard tests (Fig. 13), which suggests that these artefacts do not arise as a result of the

589   survey geometry. They may instead arise from the presence of out-of-plane arrivals affecting

590   the FWI, and cycle-skipping in the longer-offset data that is not corrected during FWI

591   (e.g. -14.92 km in Fig. 11C and I). While random noise within field data will be attenuated

592   through the FWI process, coherent noise, such as that from multiple energy, can be mapped

593   into false velocity structure (Pratt *et al.* 1998). It is difficult to determine where such artefacts

594   are to be expected, other than using qualitative model assessments, such as comparisons with

595   reflection imaging.

596   The final velocity model appears to have been resolved well in areas with seismic velocities

597   within the fault blocks of 2.80 – 5.20 km s^{-1} for the syn- and pre-rift sediments, 5.20 –

598   6.50 km s^{-1} for crystalline basement, and 6.50 – 8.50 km s^{-1} for the uppermost mantle, directly

599   below the S-reflector. These typical unit velocities, and their associated boundary velocities,

600   enable us to reinterpret the reflection seismic image. Previous interpretations have failed to

601   identify continental fault block B7 (e.g. Borgmeyer 2010), or have interpreted it to be a

602   completely pre / syn-rift sedimentary unit, above the S-reflector (Fig. 15G). However, seismic

603   velocities indicative of crystalline basement (~ 6.00 km s^{-1}) allow us to reinterpret the reflection

604   horizons in this fault block. Where previous interpretations had indicated the presence of the

605   intra syn-rift reflector we now interpret this as the top of crystalline basement, and the intra

606   syn-rift reflector is reinterpreted above, along a reflector near the ~ 4.90 km s^{-1} velocity

607   contour. We have also reinterpreted the intra syn-rift reflector in fault block B6 (Fig. 15H).

608   Velocities in this unit do not support the reflector pinching out to the west, as originally

609   suggested, but instead suggest that it maintains a consistent thickness, following a consistent

610   velocity of ~ 4.90 km s^{-1} and matches a prominent reflector in the seismic image. Additionally,

25

611   the intra syn-rift reflector is reinterpreted between fault F6a and the newly interpreted fault

612   (Fig. 15H).

613   The interpretation of the smallest continental fault block, B7, agrees with the sequential faulting

614   model, which predicts that the continental blocks decrease in size oceanward. However, the

615   interpretation of previously unidentified normal faulting, combined with the observation of

616   irregular basement and syn-rift velocities, within previously identified fault blocks (see

617   Fig. 15H) indicates that the pattern of deformation within the hyperextended domain is more

618   complicated than that described by the sequential faulting model. These interpretations could

619   suggest that there was an earlier phase of faulting, which has subsequently been overprinted by

620   the large dominant normal faults which are observed in the reflection seismic images. Such

621   interpretations would give favour to polyphase faulting models, which describe complex fault

622   overprinting, and contradict the sequential faulting model.

623   **4.2   S-reflector and associated velocities**

624   The S-reflector represents a significant velocity contrast between rocks of the lower-crust

625   juxtaposed against upper-mantle peridotites which have been serpentinised to varying degrees.

626   Our starting model exhibits a relatively low velocity contrast across the S-reflector, which is

627   the result of the smooth nature of the travel-time tomography modelling. However, we see a

628   sharpening of the velocity contrast over the S-reflector in the FWI model, indicating that the

629   velocities directly above and below the fault surface are being resolved to a greater degree.

630   This is particularly well observed below fault blocks B4, B5 and B6a, where the average

631   velocity contrasts (difference between velocities 50 ms above and below the mapped S-

632   reflector surface) increase from 0.25, 0.39, and 0.39 km s^{-1}, to 0.50, 0.68, and 0.55 km s^{-1},

633   respectively. In reality, the velocity contrast across the S-reflector is likely to be sharper than

26

634   that observed in Figures 14E and 15G-H, however, the resolution of the FWI is limited by the

635   relatively low inversion frequencies used (3.0 – 5.2 Hz).

636   It is difficult to gauge from the 2D velocity plots whether there has been an improvement in

637   the velocities associated with serpentinisation of upper mantle peridotite along and below the

638   S-reflector. The interaction between normal faulting and the P-wave velocities below the

639   S-reflector is more apparent plotted as velocity against distance. Velocities averaged over a

640   100 ms window below the mapped S-reflector are plotted against the profile distance, for both

641   the starting and inversion velocity model (Fig. 16). The starting model exhibits a general

642   pattern of preferential mantle serpentinisation, which is observed as relative decreases in the

643   seismic velocity down-dip of normal faults (Davy *et al.* 2016). This trend is particularly evident

644   down-dip of faults F6 and F7. However, in this model slight increases in the velocity down-dip

645   of faults F5 and F6a can be observed, before the expected velocity decrease. These velocity

646   increases, despite being minor, contradict the hypothesis of preferential hydration and

647   serpentinisation of the mantle by normal faulting.

648   In the same figure it can be seen that the FWI result has resolved the pattern of preferential

649   mantle serpentinisation in greater detail. Decreases in seismic velocity are now seen directly

650   down-dip of normal faults, F5 – F8 (Fig. 16). This result is more consistent than the starting

651   model with the hypothesis that normal faults act as conduits, enabling the preferential hydration

652   and serpentinisation of upper mantle peridotites below the S-reflector (Bayrakci *et al.* 2016;

653   Davy *et al.* 2016). We interpret the consistently low velocities between faults F4 and F5 to be

654   indicative of crustal material, and interpret the S-reflector as being intra-crustal in this region

655   of the model. Despite this promising result, there are unexpected features in the velocity profile

656   of the FWI model.

27

657 We observe two short-wavelength (~ 2 km) feature which show anomalously rapid change in

658 seismic velocity (highlighted by red dashed ellipsoid in Fig. 16). The most prominent exhibits

659 an increase in velocity of ~ 1.5 km s^{-1} at 41 km profile distance. This rapid change appears to

660 be particularly anomalous, when compared with the rest of the profile, and differs greatly from

661 the velocity trend in both the starting and inversion models. The other anomalous feature is

662 coincident with fault F5, and reaches the model's maximum allowed velocity of 8.50 km s^{-1}.

663 We expect the velocity of unaltered upper mantle peridotite to be ~ 8.00 km s^{-1}, thus making

664 this observation implausible (e.g., Carlson and Miller 2003). These features appear to be

665 artefacts introduced during the FWI process. It is possible that these features arise due to the

666 sparsity of data available in this experiment, or are the result of the FWI process trying to map

667 coherent noise into the velocity model.

668 Unfortunately, in order to resolve the velocity structure at these depths, we had to include data

669 that were starting to be affected by coherent multiple noise from the previous seismic shot.

670 Increasing the time between shots would enable greater depth resolution, at the expense of

671 degrading the 3D reflection image that was the primary aim of the experiment. Ignoring these

672 anomalous short-wavelength features, we can attempt to quantify the levels of observed

673 serpentinisation. Relative velocity decreases (from the normal fault to the nearest down-dip

674 velocity minima) of ~0.60 km s^{-1}, ~0.60 km s^{-1}, ~0.70 km s^{-1} and ~1.0 km s^{-1} are observed for

675 faults F5, F6a, F6 and F7, respectively. Using the study of Carlson and Miller (2003) we can

676 approximate the extent of mantle peridotite serpentinisation, based on the observed P-wave

677 velocities. Down-dip of these faults we calculate the degree of serpentinisation, averaged over

678 the resolution length of the FWI, to change from 0 to 20%, 30 to 40%, 30 to 50% and 30 to

679 60%, for faults F5, F6a, F6 and F7, respectively.

680

28

5 Conclusions

The application of FWI has yielded a clear improvement over travel-time tomography results. From this study we find that:

- FWI can be applied to sparse and noisy OBS data in deep water environments, for the purpose of producing high-resolution velocity models of shallow (< 10 km below seafloor) crustal targets.

- The final FWI result is limited by the sparsity of data available, and the presence of coherent noise at longer data offsets.

- The final velocity model exhibits a significant increase in resolution within the continental fault blocks of this hyperextended domain. This improvement in the velocity model has enabled the reinterpretation of the reflection seismic image

- Newly interpreted faults, within the existing continental blocks, may provide evidence for an earlier phase of faulting which has subsequently been overprinted by the block bounding normal faults. Such an interpretation would lend support to polyphase models of faulting within the hyperextended domain.

- Increased resolution in the seismic velocities below the S-reflector has further defined the pattern of upper mantle serpentinisation, a result of preferential hydration by normal faults acting as water conduits. The degree of preferential mantle serpentinisation is interpreted to vary between 20 – 60%.

Given a more optimised seismic shooting period we can expect that the results would have shown an even greater quality. Increasing the time between subsequent seismic shots would allow time for energy of the previous shot to dissipate, reducing the coherent noise in the recorded data and enabling greater depth resolution of the FWI method. We suggest that future marine studies, targeting crustal structure, take into consideration the application of FWI to

29

705 their proposed datasets. While a higher density of OBS/H is desirable, we have shown that a

706 relatively sparse profile can improve the resolution of travel-time tomography models. This

707 approach will also allow for the improved migration of reflection seismic images, which was

708 not investigated here. There may also be merit in applying the FWI method to existing high

709 quality 2D OBS/H datasets where high quality travel-time tomography models have already

710 been determined.

6   Acknowledgements

References

724 Arnoux, G.M., Toomey, D.R., Hooft, E.E., Wilcock, W.S., Morgan, J., Warner, M. & VanderBeek, B.P.,
725   2017. Seismic evidence that black smoker heat flux is influenced by localized magma
726   replenishment and associated increases in crustal permeability, *Geophysical Research Letters,*
727   44**,** 1687-1695.
728 Bayrakci, G., Minshull, T., Sawyer, D., Reston, T.J., Klaeschen, D., Papenberg, C., Ranero, C., Bull, J.,
729   Davy, R. & Shillington, D., 2016. Fault-controlled hydration of the upper mantle during
730   continental rifting, *Nature Geoscience,* 9**,** 384-388.
731 Beslier, M.-O., Ask, M. & Boillot, G., 1993. Ocean-continent boundary in the Iberia Abyssal Plain from
732   multichannel seismic data, *Tectonophysics,* 218**,** 383-393.

733   Boillot, G., Winterer, E. & Meyer, A., 1987. Introduction, objectives, and principal results: Ocean
734   Drilling Program Leg 103, west Galicia Margin, *Proc. Ocean Drill. Program, Initial Reports,* 103**,**
735   3-17.
736   Borgmeyer, A.L., 2010. Three-dimensional geometries of rifting on a hyperextended margin-
737   Interpretation of seismic reflection profiles from the Deep Galicia Basin, Iberia, MSc thesis
738   MSc, Rice University.
739   Brossier, R., Operto, S. & Virieux, J., 2009. Seismic imaging of complex onshore structures by 2D elastic
740   frequency-domain full-waveform inversion, *Geophysics,* 74**,** WCC105-WCC118.
741   Bunks, C., Saleck, F.M., Zaleski, S. & Chavent, G., 1995. Multiscale seismic waveform inversion,
742   *Geophysics,* 60**,** 1457-1473.
743   Carlson, R.L. & Miller, D.J., 2003. Mantle wedge water contents estimated from seismic velocities in
744   partially serpentinized peridotites, *Geophysical Research Letters,* 30**,** 1250.
745   Davy, R., Minshull, T., Bayrakci, G., Bull, J., Klaeschen, D., Papenberg, C., Reston, T.J., Sawyer, D. & Zelt,
746   C., 2016. Continental hyperextension, mantle exhumation, and thin oceanic crust at the
747   continent-ocean transition, West Iberia: New insights from wide-angle seismic, *Journal of
748   Geophysical Research: Solid Earth,* 121**,** 3177-3199.
749   Dean, S., Sawyer, D. & Morgan, J., 2015. Galicia Bank ocean–continent transition zone: New seismic
750   reflection constraints, *Earth and Planetary Science Letters,* 413**,** 197-207.
751   Dessa, J.X., Operto, S., Kodaira, S., Nakanishi, A., Pascal, G., Virieux, J. & Kaneda, Y., 2004. Multiscale
752   seismic imaging of the eastern Nankai trough by full waveform inversion, *Geophysical
753   Research Letters,* 31**,** L18606.
754   Gardner, G., Gardner, L. & Gregory, A., 1974. Formation velocity and density—The diagnostic basics
755   for stratigraphic traps, *Geophysics,* 39**,** 770-780.
756   Jaiswal, P., Zelt, C.A., Bally, A.W. & Dasgupta, R., 2008. 2-D traveltime and waveform inversion for
757   improved seismic imaging: Naga Thrust and Fold Belt, India, *Geophysical Journal International,*
758   173**,** 642-658.
759   Jones, C., Evans, M., Ratcliffe, A., Conroy, G., Jupp, R., Selvage, J. & Ramsey, L., 2013. Full waveform
760   inversion in a complex geological setting-a narrow azimuth towed streamer case study from
761   the Barents Sea. *in Proceedings of the 75th EAGE Conference*, Extended Abstracts.
762   Kamei, R., Pratt, R.G. & Tsuji, T., 2012. Waveform tomography imaging of a megasplay fault system in
763   the seismogenic Nankai subduction zone, *Earth and Planetary Science Letters,* 317**,** 343-353.
764   Kapoor, S., Vigh, D., Wiarda, E. & Alwon, S., 2013. Full waveform inversion around the world. *in
765   Proceedings of the 75th EAGE Conference*, Extended Abstracts, doi: 10.3997/2214-
766   4609.20130827.
767   Kolb, P., Collino, F. & Lailly, P., 1986. Pre-stack inversion of a 1-D medium, *Proceedings of the IEEE,* 74**,**
768   498-508.
769   Korenaga, J., Holbrook, W., Kent, G., Kelemen, P., Detrick, R., Larsen, H.C., Hopper, J. & Dahl-Jensen,
770   T., 2000. Crustal structure of the southeast Greenland margin from joint refraction and
771   reflection seismic tomography, *Journal of Geophysical Research: Solid Earth,* 105**,** 21591-
772   21614.
773   Lailly, P., 1983. The seismic inverse problem as a sequence of before stack migrations. *in Conference
774   on Inverse Scattering: Theory and Application*, ed J. Bee Bednar, R. R., Enders Robinson. Soc.
775   Industr. Appl. Math., Philadelphia.
776   McDermott, K. & Reston, T., 2015. To see, or not to see? Rifted margin extension, *Geology,* 43**,** 967-
777   970.
778   Minshull, T.A., Sinha, M.C. & Peirce, C., 2005. Multi-disciplinary, sub-seabed geophysical imaging, *Sea
779   Technology,* 46**,** 27-31.
780   Mispel, J., Houbiers, M., Knudsen, B. & Amundsen, L., 2013. FWI with OBC Data From the Mariner
781   Field, UK-The Impact on Mapping Sands at Reservoir Level. *in Proceedings of the 75th EAGE
782   Conference*, Extended Abstracts, doi: 10.3997/2214-4609.20130829.

783 Morgan, J., Warner, M., Arnoux, G., Hooft, E., Toomey, D., VanderBeek, B. & Wilcock, W., 2016. Next-
784   generation seismic experiments–II: wide-angle, multi-azimuth, 3-D, full-waveform inversion
785   of sparse field data, *Geophysical Journal International,* 204**,** 1342-1363.
786 Morgan, J., Warner, M., Bell, R., Ashley, J., Barnes, D., Little, R., Roele, K. & Jones, C., 2013. Next-
787   generation seismic experiments: wide-angle, multi-azimuth, three-dimensional, full-
788   waveform inversion, *Geophysical Journal International,* 195**,** 1657-1678.
789 Mothi, S., Schwarz, K. & Zhu, H., 2013. Impact of full-azimuth and long-offset acquisition on Full
790   Waveform Inversion in deep water Gulf of Mexico. *in Proceedings of the 75th EAGE*
791   *Conference*, Extended Abstracts, doi: 10.1190/segam2013-0102.1.
792 Operto, S., Virieux, J., Amestoy, P., L'Excellent, J.-Y., Giraud, L. & Ali, H.B.H., 2007. 3D finite-difference
793   frequency-domain modeling of visco-acoustic wave propagation using a massively parallel
794   direct solver: A feasibility study, *Geophysics,* 72**,** SM195-SM211.
795 Operto, S., Virieux, J., Dessa, J.X. & Pascal, G., 2006. Crustal seismic imaging from multifold ocean
796   bottom seismometer data by frequency domain full waveform tomography: Application to
797   the eastern Nankai trough, *Journal of Geophysical Research: Solid Earth,* 111**,** B09306.
798 Pérez-Gussinyé, M., 2013. A tectonic model for hyperextension at magma-poor rifted margins: an
799   example from the West Iberia–Newfoundland conjugate margins, *Geological Society, London,*
800   *Special Publications,* 369**,** 403-427.
801 Pérez-Gussinyé, M., Ranero, C., Reston, T.J. & Sawyer, D., 2003. Mechanisms of extension at
802   nonvolcanic margins: Evidence from the Galicia interior basin, west of Iberia, *Journal of*
803   *Geophysical Research: Solid Earth,* 108**,** 2245.
804 Pérez-Gussinyé, M. & Reston, T.J., 2001. Rheological evolution during extension at nonvolcanic rifted
805   margins: onset of serpentinization and development of detachments leading to continental
806   breakup, *Journal of Geophysical Research: Solid Earth,* 106**,** 3961-3975.
807 Pratt, R.G., 1999. Seismic waveform inversion in the frequency domain, Part 1: Theory and verification
808   in a physical scale model, *Geophysics,* 64**,** 888-901.
809 Pratt, R.G., Shin, C. & Hick, G., 1998. Gauss–Newton and full Newton methods in frequency–space
810   seismic waveform inversion, *Geophysical Journal International,* 133**,** 341-362.
811 Ranero, C.R. & Pérez-Gussinyé, M., 2010. Sequential faulting explains the asymmetry and extension
812   discrepancy of conjugate margins, *Nature,* 468**,** 294-299.
813 Ratcliffe, A., Win, C., Vinje, V., Conroy, G., Warner, M., Umpleby, A., Stekl, I., Nangoo, T. & Bertrand,
814   A., 2011. Full waveform inversion: A North Sea OBC case study. *in 2011 SEG Annual Meeting,*
815   Society of Exploration Geophysicists, Expanded Abstracts 30, pp. 2384–2388.
816 Reston, T. & McDermott, K., 2014. An assessment of the cause of the 'extension discrepancy'with
817   reference to the west Galicia margin, *Basin Research,* 26**,** 135-153.
818 Reston, T.J., 2009. The structure, evolution and symmetry of the magma-poor rifted margins of the
819   North and Central Atlantic: a synthesis, *Tectonophysics,* 468**,** 6-27.
820 Reston, T.J., Leythäuser, T., Booth-Rea, G., Sawyer, D., Klaeschen, D. & Long, C., 2007. Movement along
821   a low-angle normal fault: The S reflector west of Spain, *Geochemistry, Geophysics,*
822   *Geosystems,* 8**,** Q06002.
823 Sawyer, D.S., Reston, T., Gussinye, M.P., Zelt, C.A., Austin, J.A., Nakamura, Y., Danobeitia, J. & Cordoba,
824   D., 1997. The Iberia Seismic Experiment (ISE97): MCS reflection profiles, *EOS,* 78.
825 Sirgue, L., 2006. The importance of low frequency and large offset in waveform inversion. *in*
826   *Proceedings of the 68th EAGE Conference*, Extended Abstracts, doi: 10.3997/2214-
827   4609.201402146.
828 Sirgue, L., Barkved, O., Dellinger, J., Etgen, J., Albertin, U. & Kommedal, J., 2010. Thematic set: Full
829   waveform inversion: The next leap forward in imaging at Valhall, *First Break,* 28**,** 65-70.
830 Srivastava, S., Sibuet, J.-C., Cande, S., Roest, W. & Reid, I.D., 2000. Magnetic evidence for slow seafloor
831   spreading during the formation of the Newfoundland and Iberian margins, *Earth and*
832   *Planetary Science Letters,* 182**,** 61-76.

833 Tarantola, A., 1984. Inversion of seismic reflection data in the acoustic approximation, *Geophysics,* 49**,**
834   1259-1266.
835 Tarantola, A., 1987. Inverse Problem Theory: Models for Data Fitting and Model Parameter
836   EstimationElsevier, Amsterdam.
837 Virieux, J., 1986. P-SV wave propagation in heterogeneous media: Velocity-stress finite-difference
838   method, *Geophysics,* 51**,** 889-901.
839 Virieux, J. & Operto, S., 2009. An overview of full-waveform inversion in exploration geophysics,
840   *Geophysics,* 74**,** WCC1-WCC26.
841 Warner, M., Ratcliffe, A., Nangoo, T., Morgan, J., Umpleby, A., Shah, N., Vinje, V., Štekl, I., Guasch, L.
842   & Win, C., 2013. Anisotropic 3D full-waveform inversion, *Geophysics,* 78**,** R59-R80.
843 Warner, M., Umpleby, A., Stekl, I. & Morgan, J., 2010. 3D full-wavefield tomography: imaging beneath
844   heterogeneous overburden. *in Proceedings of the 72nd EAGE Conference*, Extended Abstracts,
845   doi: 10.3997/2214-4609.20149944
846 Williamson, P., 1991. A guide to the limits of resolution imposed by scattering in ray tomography,
847   *Geophysics,* 56**,** 202-207.
848 Wu, R.-S. & Toksöz, M.N., 1987. Diffraction tomography and multisource holography applied to
849   seismic imaging, *Geophysics,* 52**,** 11-25.
850 Zelt, C.A. & Barton, P.J., 1998. Three-dimensional seismic refraction tomography: A comparison of two
851   methods applied to data from the Faeroe Basin, *Journal of Geophysical Research: Solid Earth,*
852   103**,** 7187-7210.
853 Zelt, C.A., Sain, K., Naumenko, J.V. & Sawyer, D.S., 2003. Assessment of crustal velocity models using
854   seismic refraction and reflection tomography, *Geophysical Journal International,* 153**,** 609-
855   626.

856

857 **Tables**

Inversion low-pass frequency	Reduction in misfit functional
3.0 Hz	9.2%
3.4 Hz	2.2%
3.9 Hz	2.4%
4.5 Hz	1.8%
5.2 Hz	2.5%

858 Table 1: Reduction in misfit functional for given inversion low-pass frequencies. Each

859 frequency is iterated 10 times.

860 **Figures**

861 Start on next page. Note – I have made figures as big as possible for review. Sizes to be

862 adjusted for publication.

33
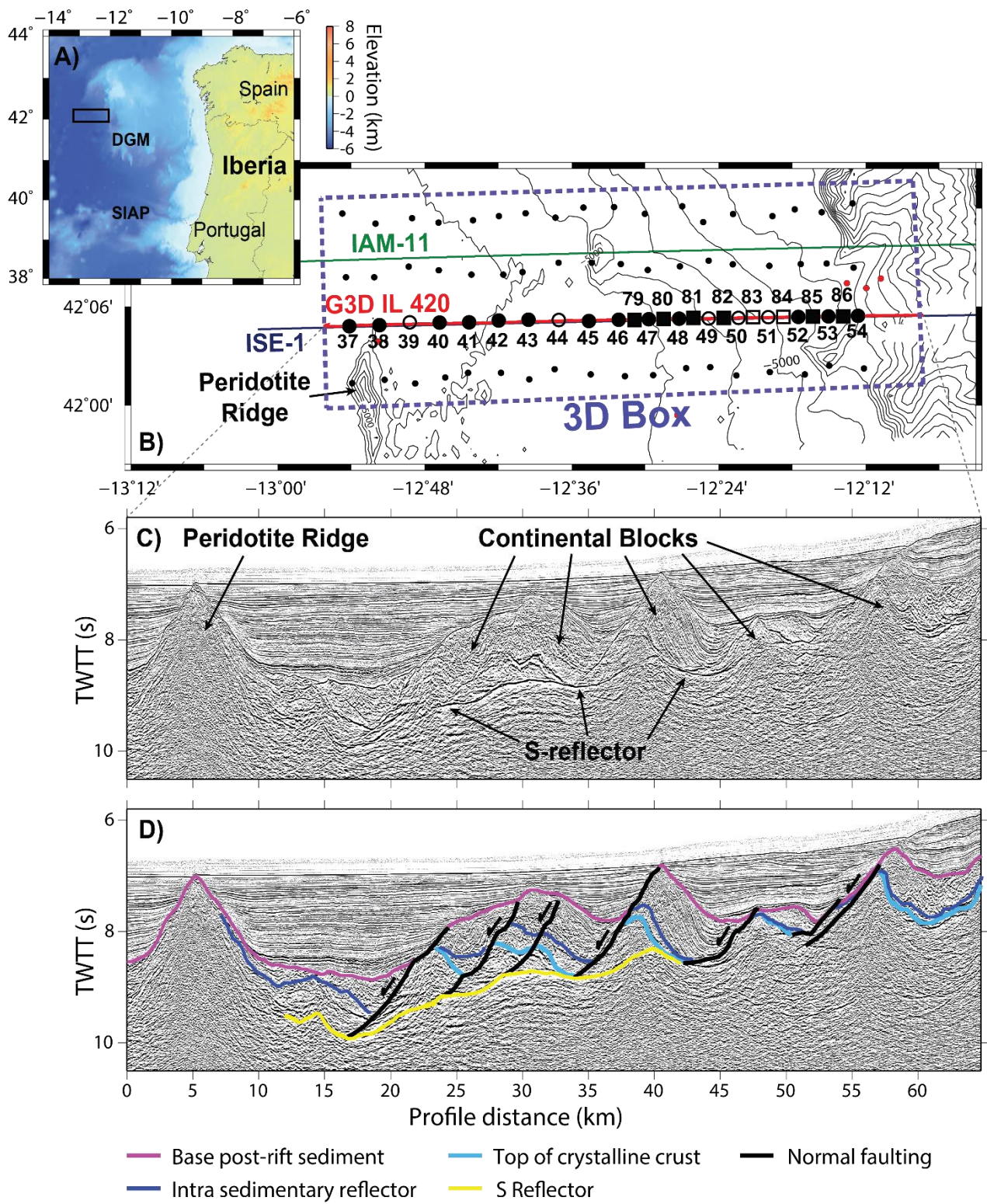
Figure 1: A) Bathymetric map of the Deep Galicia Margin (DGM) and the Southern Iberia

Abyssal Plain (SIAP) with the relative location of Fig. 1B (black rectangle). B) Map of the

Galicia-3D seismic experiment. Galicia 3-D inline 420 seismic profile is illustrated by a red

867   line; large black circles indicate the location of OBIF OBS along seismic inline 420; large black

868   squares indicate GEOMAR OBH; unfilled circles and squares indicate instruments which

869   recovered no data or were excluded from the FWI process. Purple line indicates the ISE-1

870   seismic profile; green line indicates the IAM-11 seismic profile; ODP Leg 103 sites are

871   indicated by red circles (Boillot *et al.* 1987). C) Kirchhoff pre-stack time-migrated

872   multichannel seismic reflection image of inline 420, highlighting features of the Deep Galicia

873   Margin. D) Simplified interpretation of C).
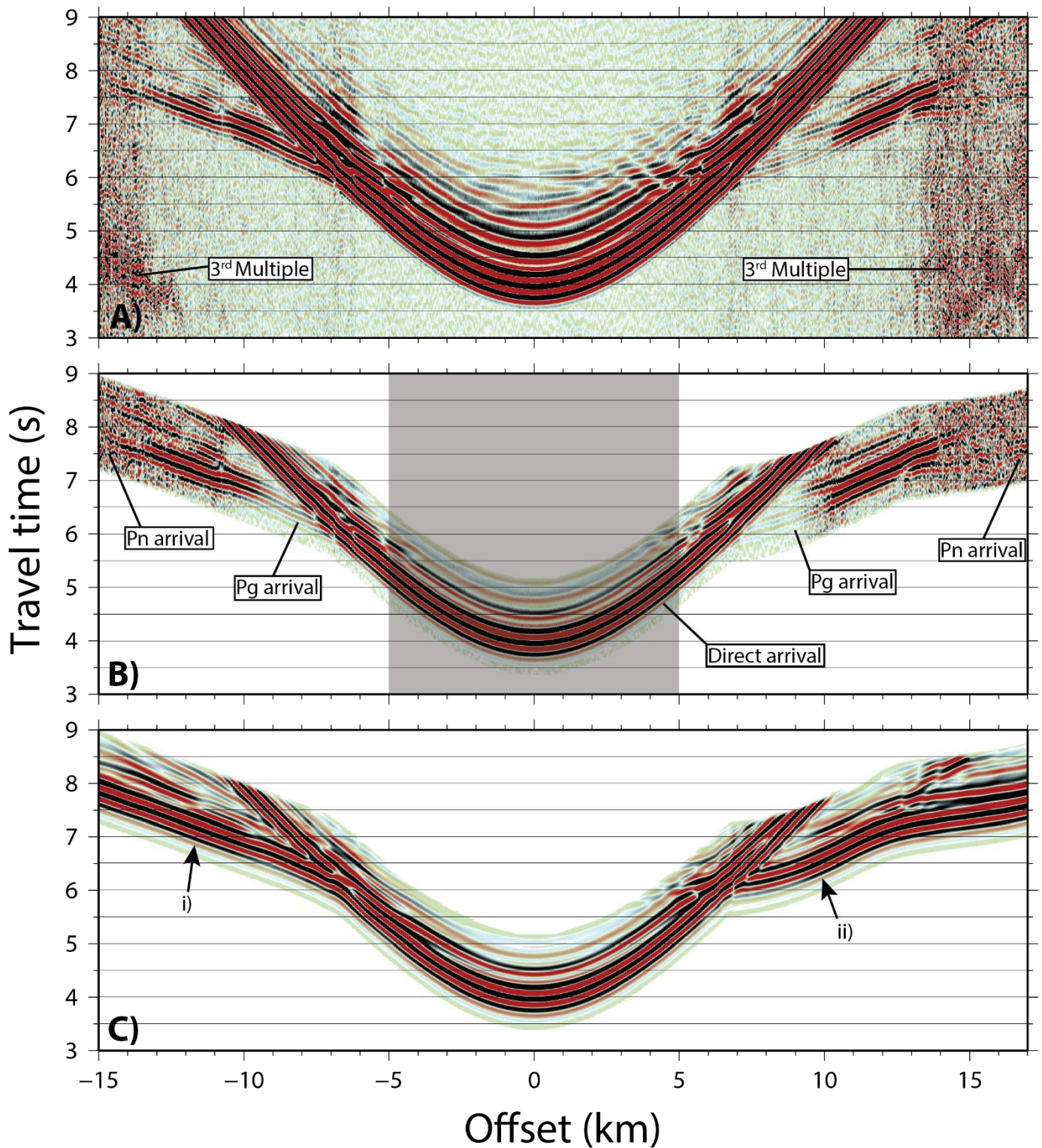
Figure 2: A) Example receiver gather from OBS 46, filtered with an Ormsby band-pass comprised of corner frequencies 2-3-4.5-6.5 Hz. The 3rd multiple from the previous seismic shot is indicated. B) Same receiver gather as in A), windowed 1.8 s after the first arrival for input into the inversion process. Grey area indicates data excluded from the inversion. Identified seismic phases are indicated. C) Synthetic receiver gather for OBS46 generated using the starting velocity model in Fig 4A.
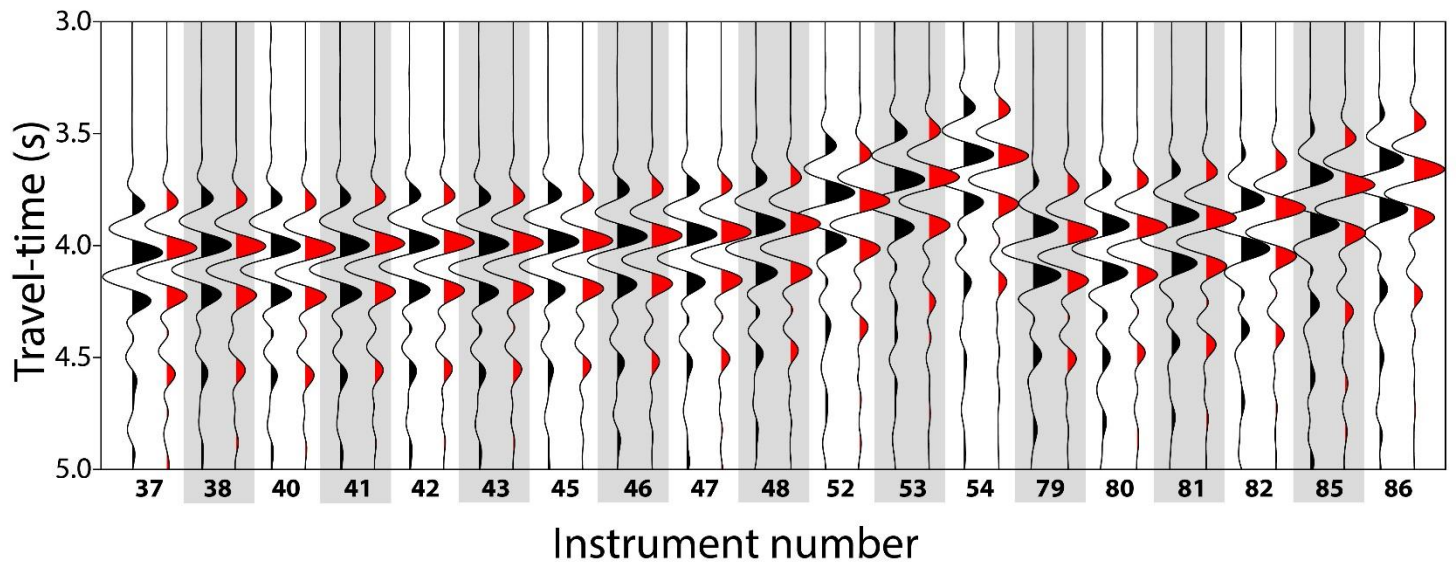
Figure 3: Fit between observed and synthetic direct water wave arrivals. Observed near-offset traces (black) compared with the equivalent synthetic trace (red) through the starting velocity model, for all instruments used in this study. Observed data are band-pass filtered (Ormsby, corner frequencies 2-3-4.5-6.5 Hz).
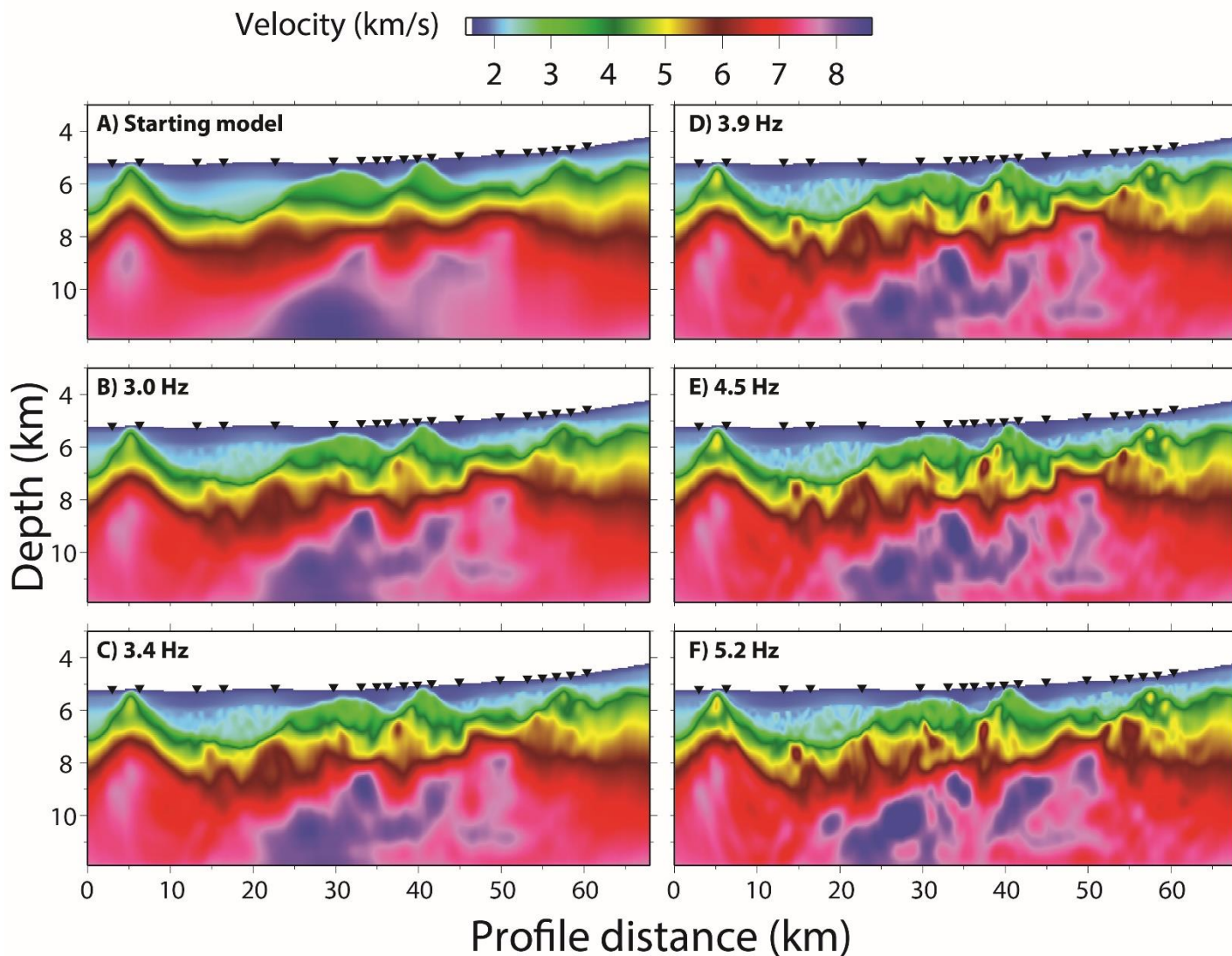
Figure 4: A) Starting velocity model input to the FWI. Results of the iterative FWI process for low-pass filter frequencies of: B) 3.0 Hz; C) 3.4 Hz; D) 3.9 Hz; E) 4.5 Hz and F) 5.2 Hz. Black upturned triangles indicate the locations of utilised instruments. Vertical exaggeration is 3.2.
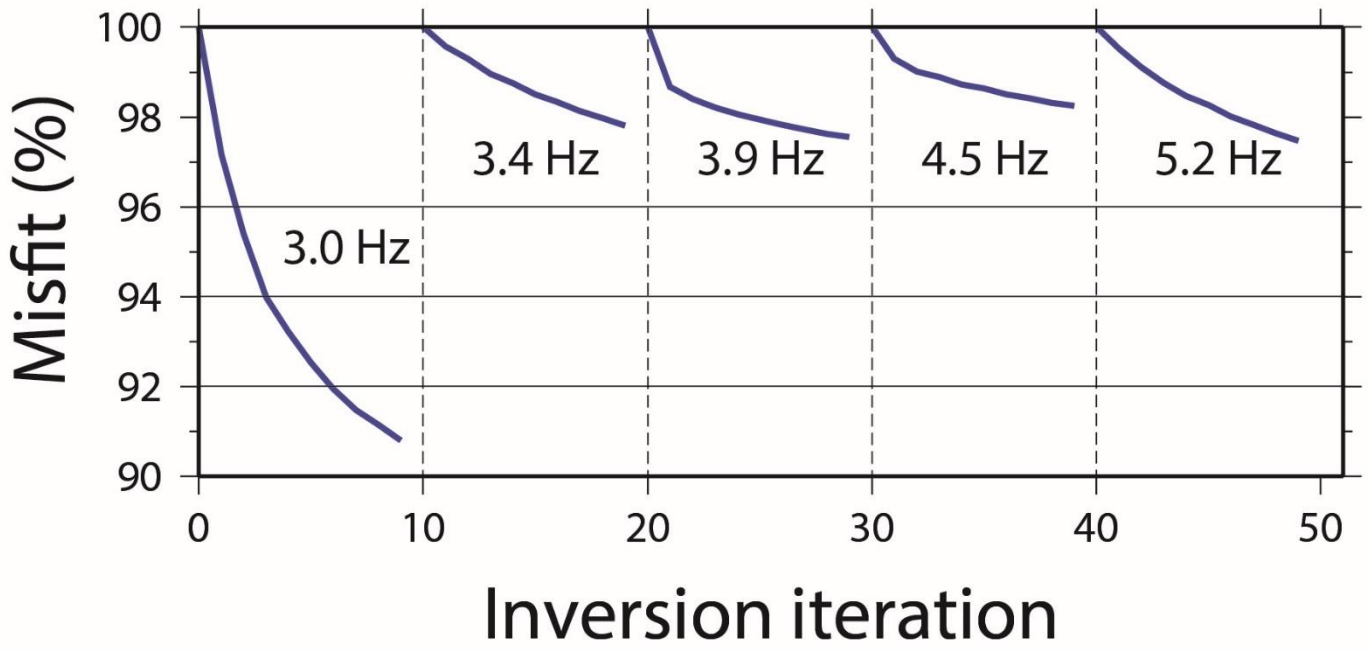
887   Figure 5: Misfit reduction versus inversion iterations for the five low-cut frequency bands, 3.0,

888   3.4, 3.9, 4.5 and 5.2 Hz.

889

890

891

892

893

894

895

896

897

898
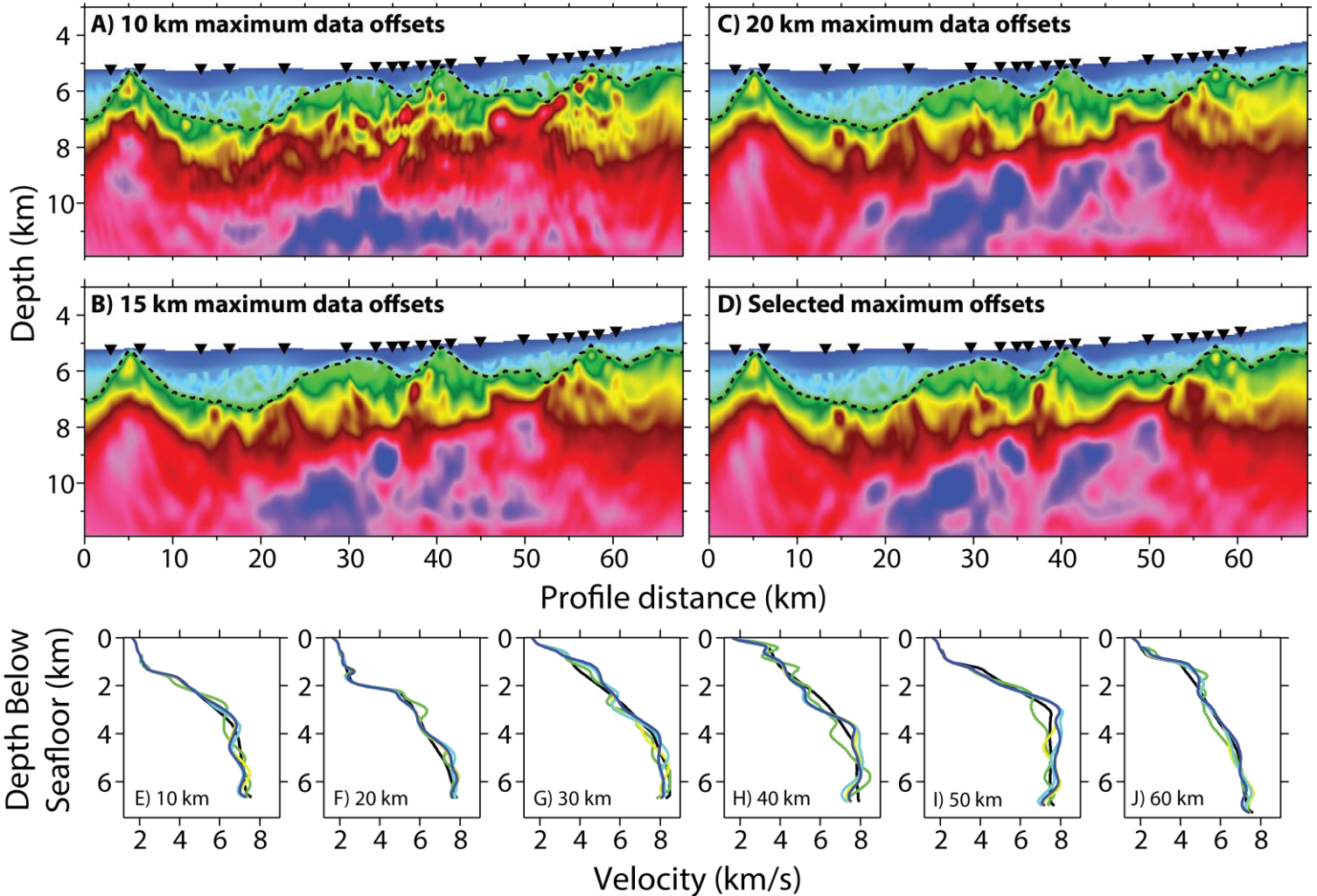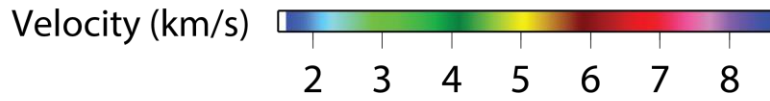
Figure 6: Inversion models for maximum data offsets of A) 10 km B) 15 km C) 20 km D) Instrument specific offsets. Black upturned triangles indicate the locations of utilised instruments, black dashed line indicates the base of post-rift sediments. Vertical exaggeration is 3.2. E-J) 1D velocity profiles through the resulting models, below the seafloor, at set profile distances (10, 20, 30, 40, 50 and 60 km, respectively). Line colours are black: starting model, green: 10 km data offsets, yellow: 15 km data offsets, light blue: 20 km data offsets, blue: instrument specific data offsets.

40
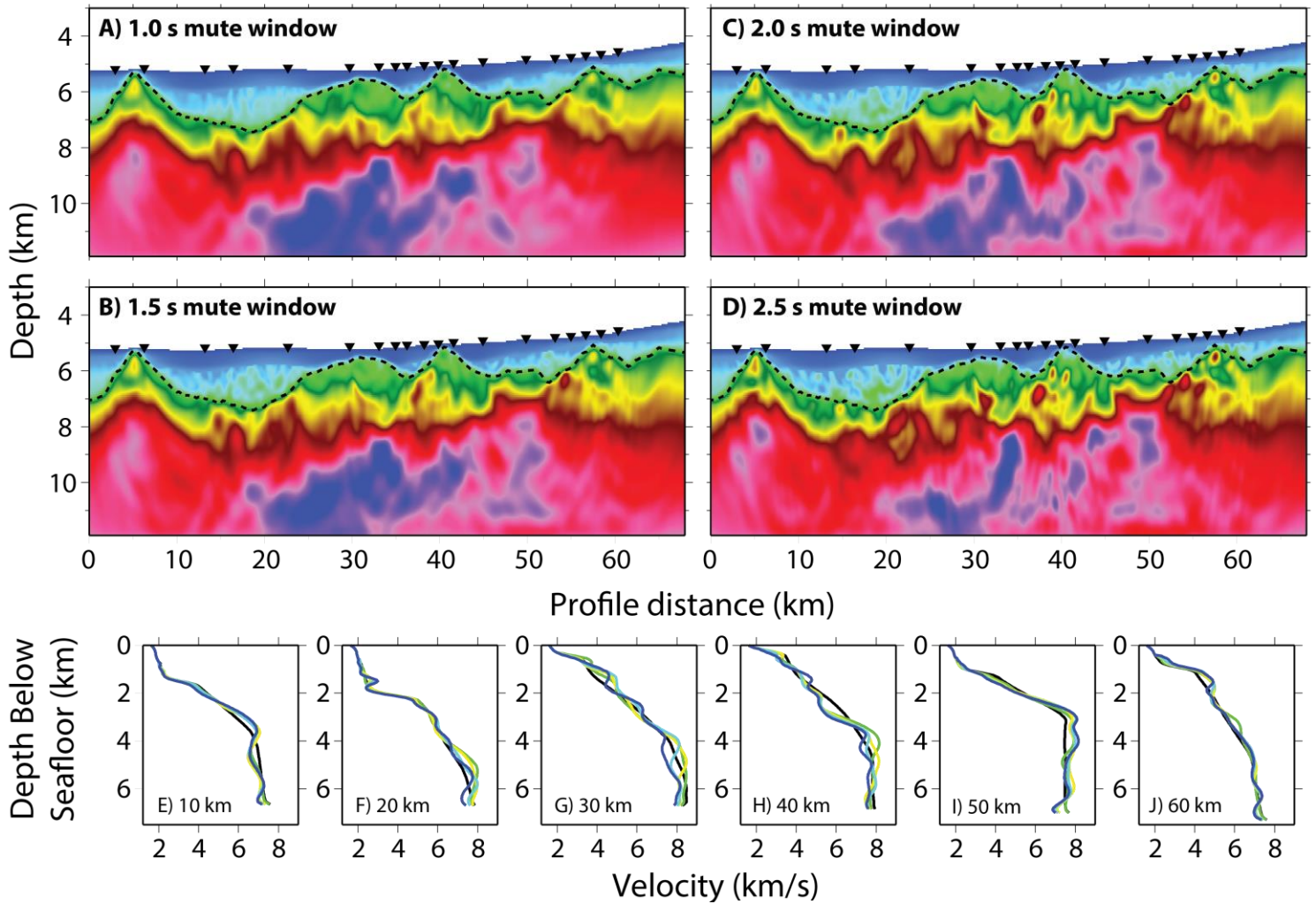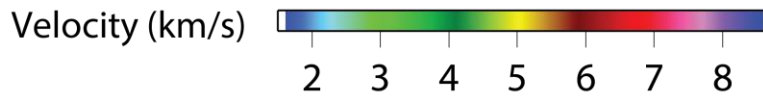
Figure 7: Inversion models for varying mute windows of A) 1.0 s B) 1.5 s C) 2.0 s D) 2.5 s. Black upturned triangles indicate the locations of utilised instruments, black dashed line indicates the base of post-rift sediments. Vertical exaggeration is 3.2. E-J) 1D velocity profiles through the resulting models, below the seafloor, at set profile distances (10, 20, 30, 40, 50 and 60 km, respectively). Line colours are black: starting model, green: 1.0 s, yellow: 1.5 s, light blue: 2.0 s, blue: 2.5 s.
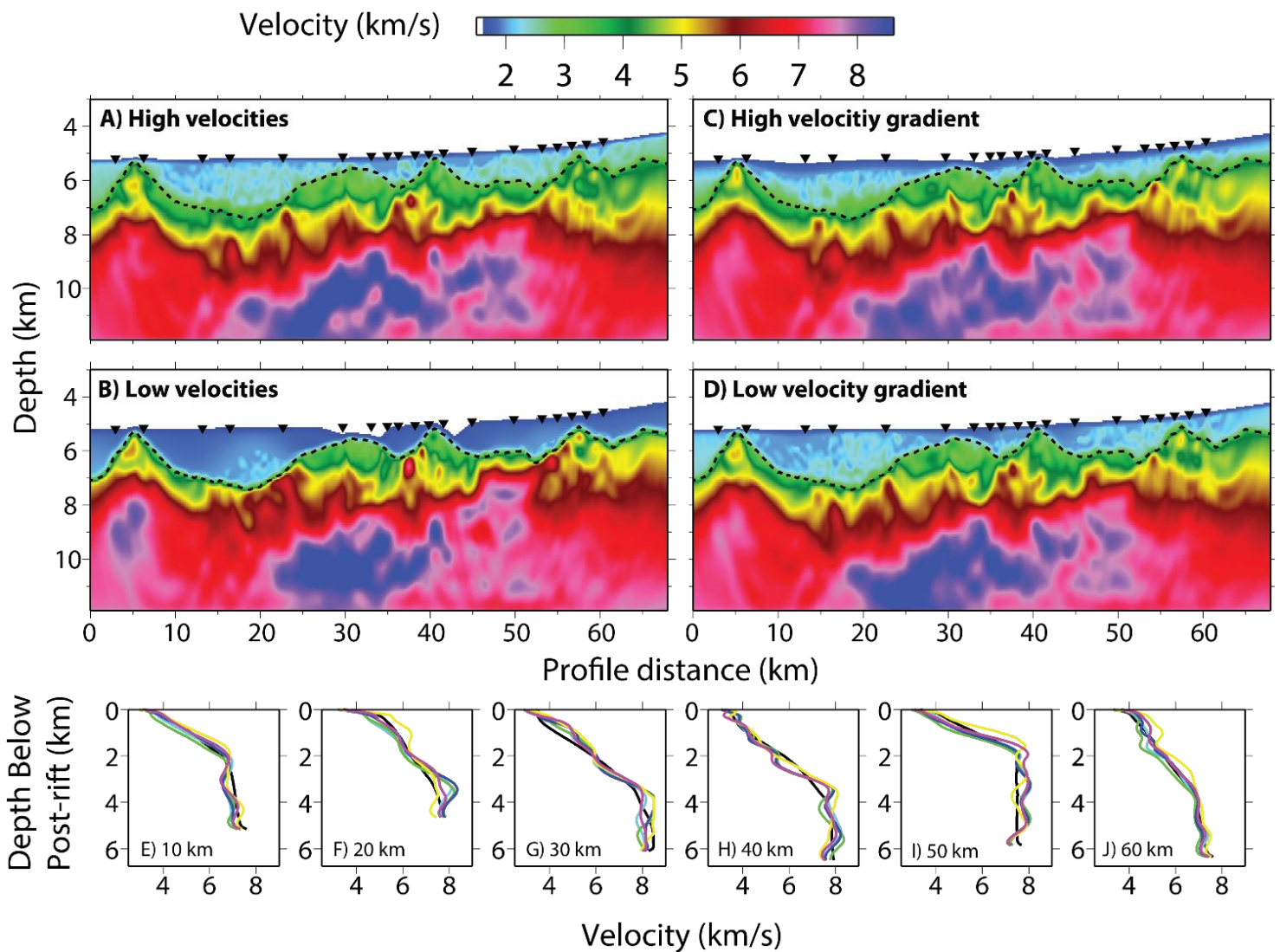
Figure 8: Inversion models for varying starting sediment velocity models, as described in section 3.7: A) High velocities B) Low velocities C) High-velocity gradient D) Low-velocity gradient. Black upturned triangles indicate the locations of utilised instruments, black dashed line indicates the base of post-rift sediments. Vertical exaggeration is 3.2. E-J) 1D velocity profiles through the resulting models, below post-rift sediment, at set profile distances (10, 20, 30, 40, 50 and 60 km, respectively). Line colours are black: starting model, green: high velocities, yellow: low velocities, light blue: high-velocity gradient, blue: low-velocity gradient.
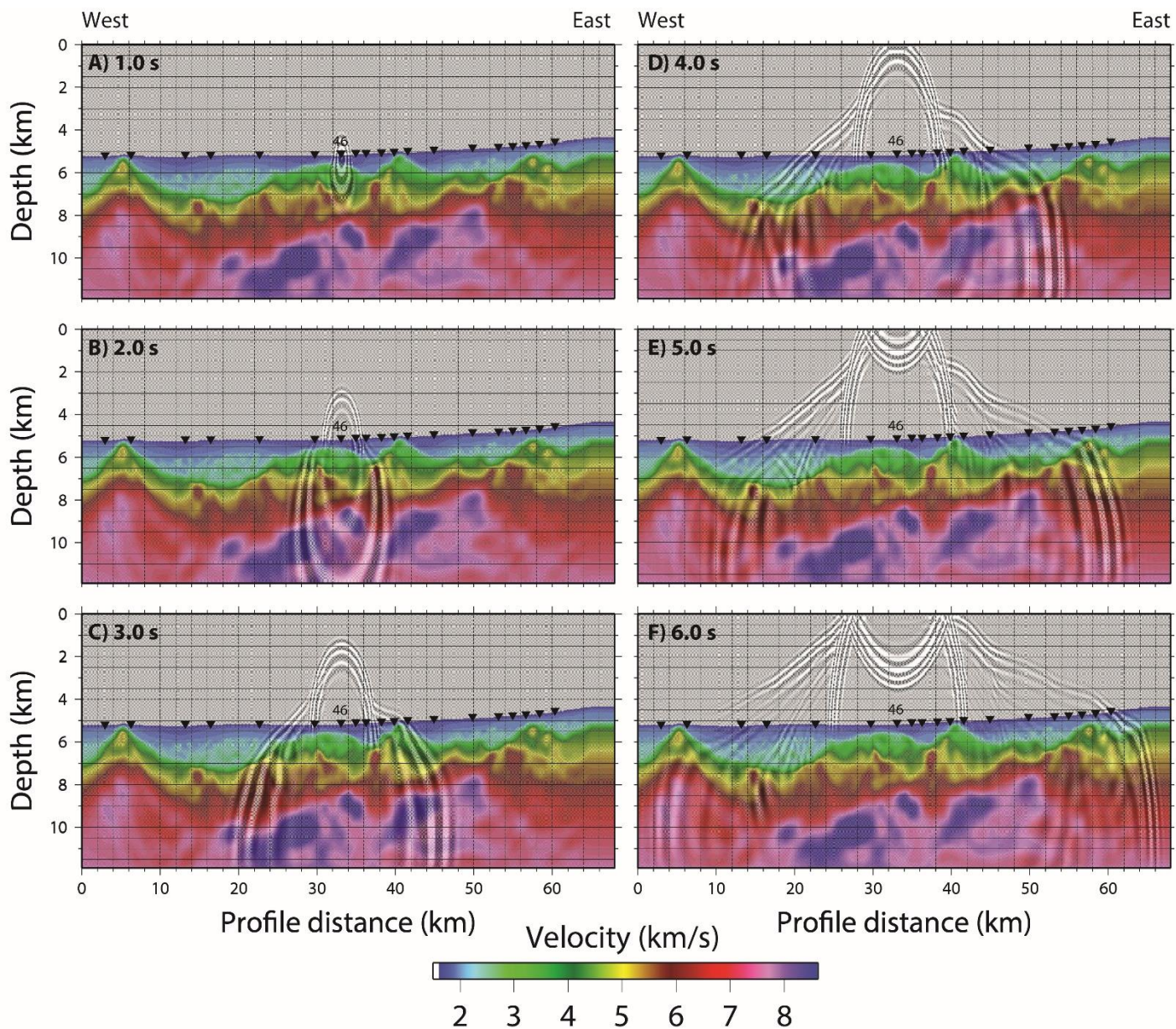
Figure 9: Propagation of the derived source wavelet through the final inversion model, originating at OBS46, at discrete times: A) 1.0 s, B) 2.0 s, C) 3.0 s, D) 4.0 s, E) 5.0 s, F) 6.0 s. Black upturned triangles indicate the locations of utilised instruments. Vertical exaggeration is 3.2.
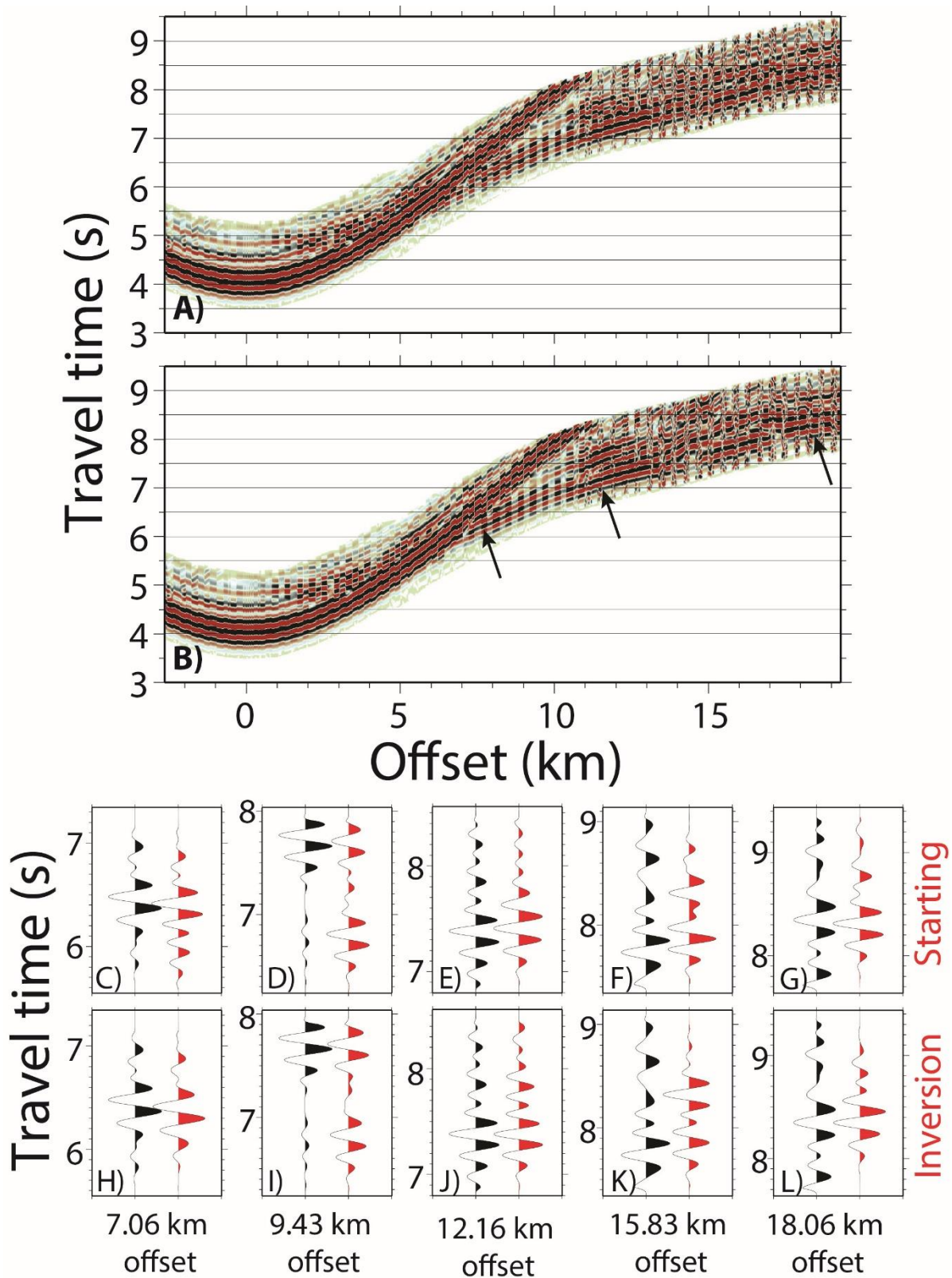
Figure 10: OBS 37. A) Observed data interleaved with synthetic through the starting model in alternative offset bins of 200 m. B) Observed data interleaved with synthetic through the inversion model in alternative offset bins of 200 m. C-G) Black traces: observed data, red traces: synthetic data through the starting model. H-L) Black traces: observed data, red traces: synthetic data through the FWI model.
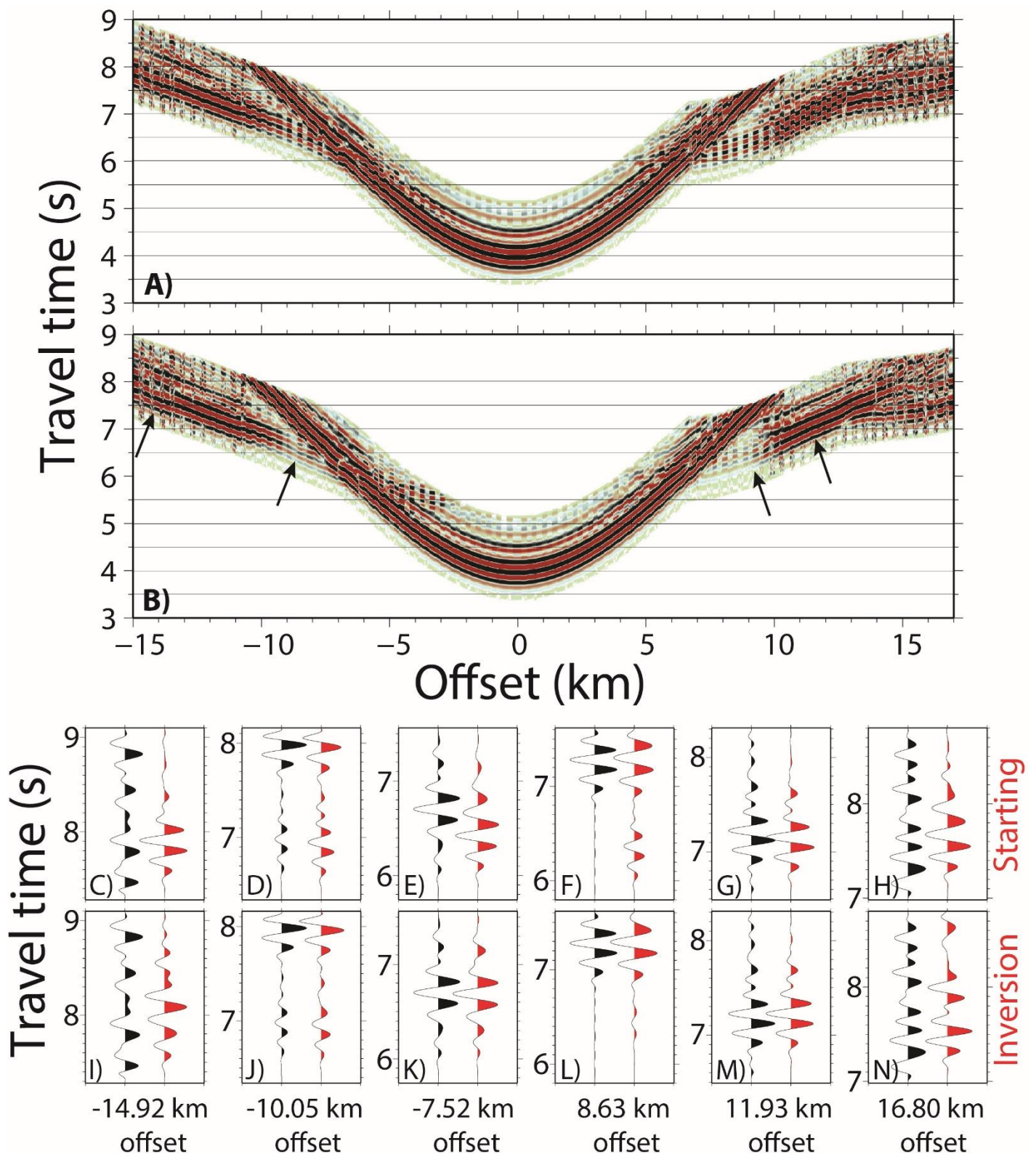
44

Figure 11: OBS 46. A) Observed data interleaved with synthetic through the starting model in alternative offset bins of 200 m. B) Observed data interleaved with synthetic through the inversion model in alternative offset bins of 200 m. C-H) Black traces: observed data, red traces: synthetic data through the starting model. I-N) Black traces: observed data, red traces: synthetic data through the FWI model.

45
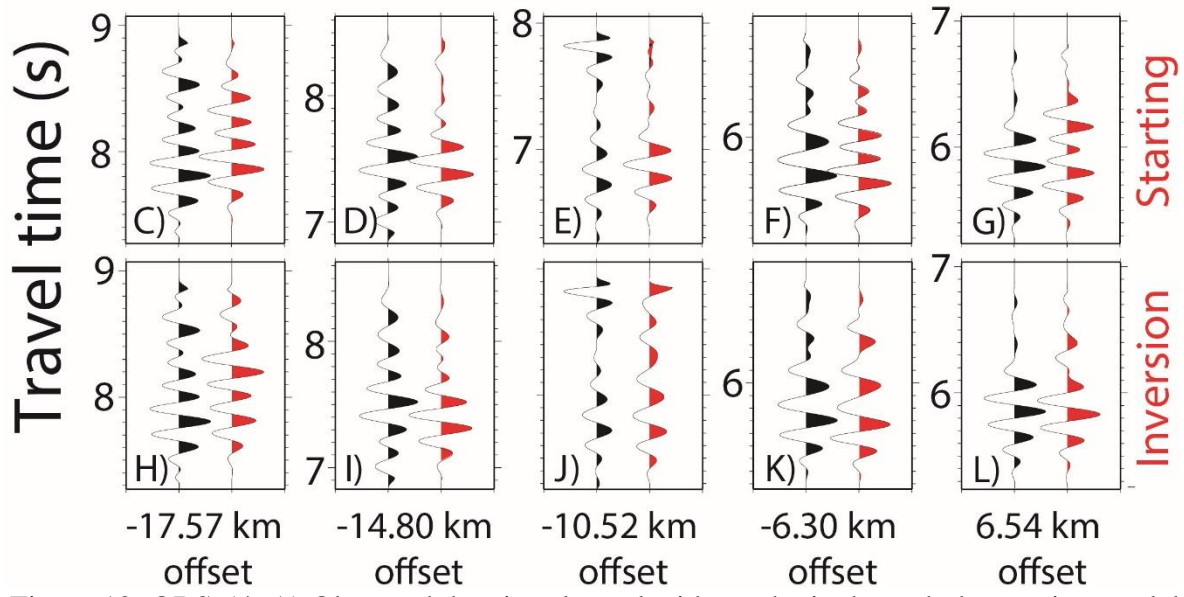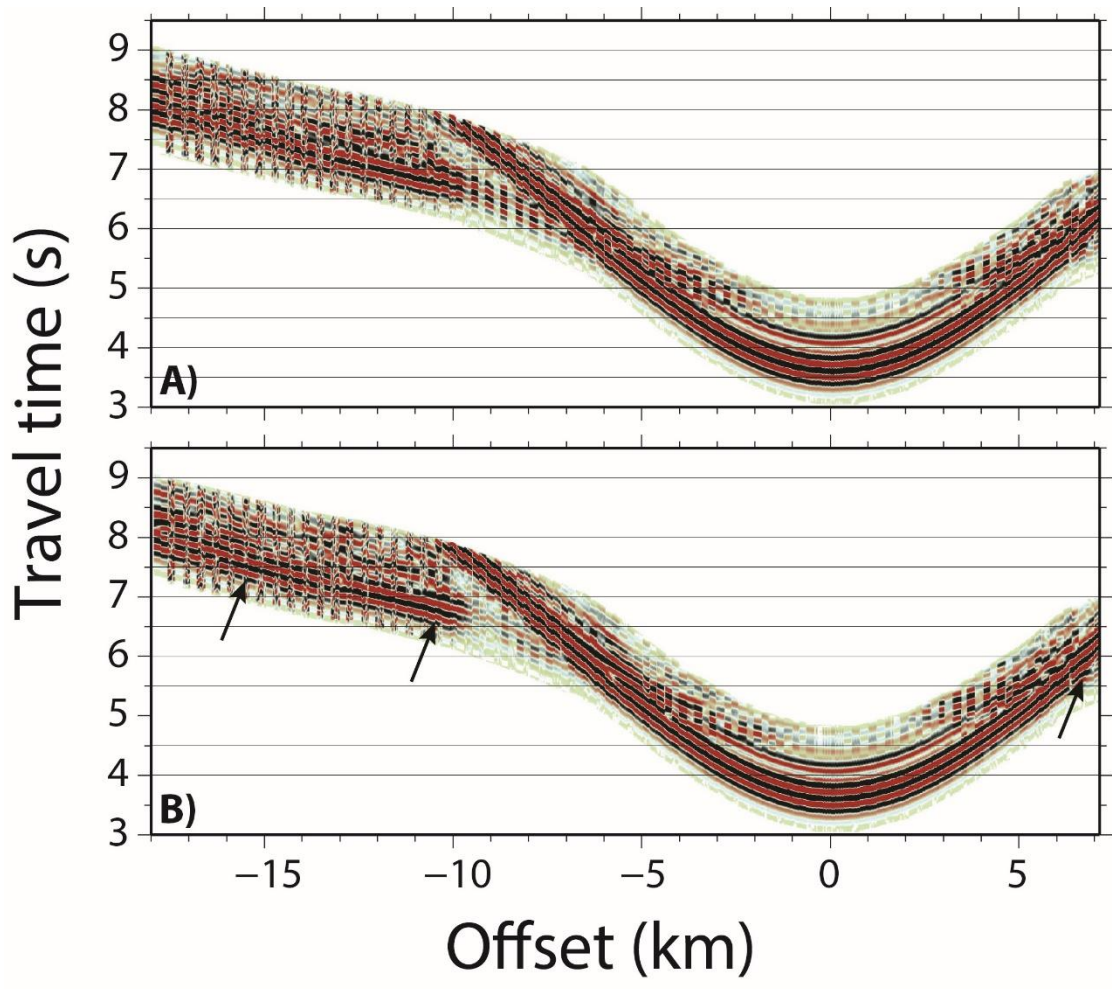
Figure 12: OBS 54. A) Observed data interleaved with synthetic through the starting model in alternative offset bins of 200 m. B) Observed data interleaved with synthetic through the inversion model in alternative offset bins of 200 m. C-G) Black traces: observed data, red traces: synthetic data through the starting model. H-L) Black traces: observed data, red traces: synthetic data through the FWI model.

46

946
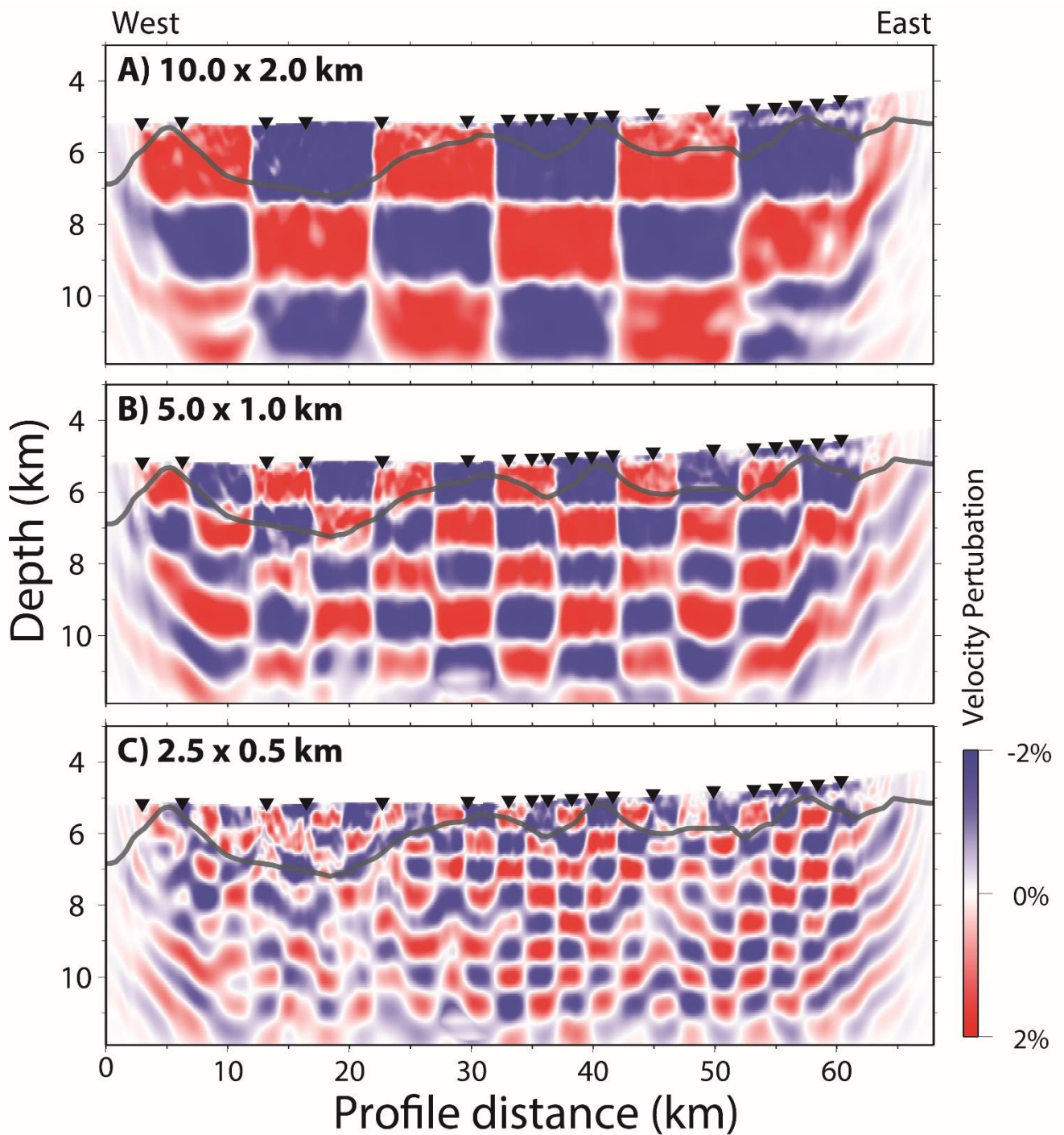
Figure 13: Checkerboard resolution test results. Anomaly check dimensions: A) 10.0 x 2.0 km,

B) 5.0 x 1.0 km, C) 2.0 x 0.5 km. Vertical exaggeration is 3.4. Grey line represents the top of

the syn-rift sediments.

950

951
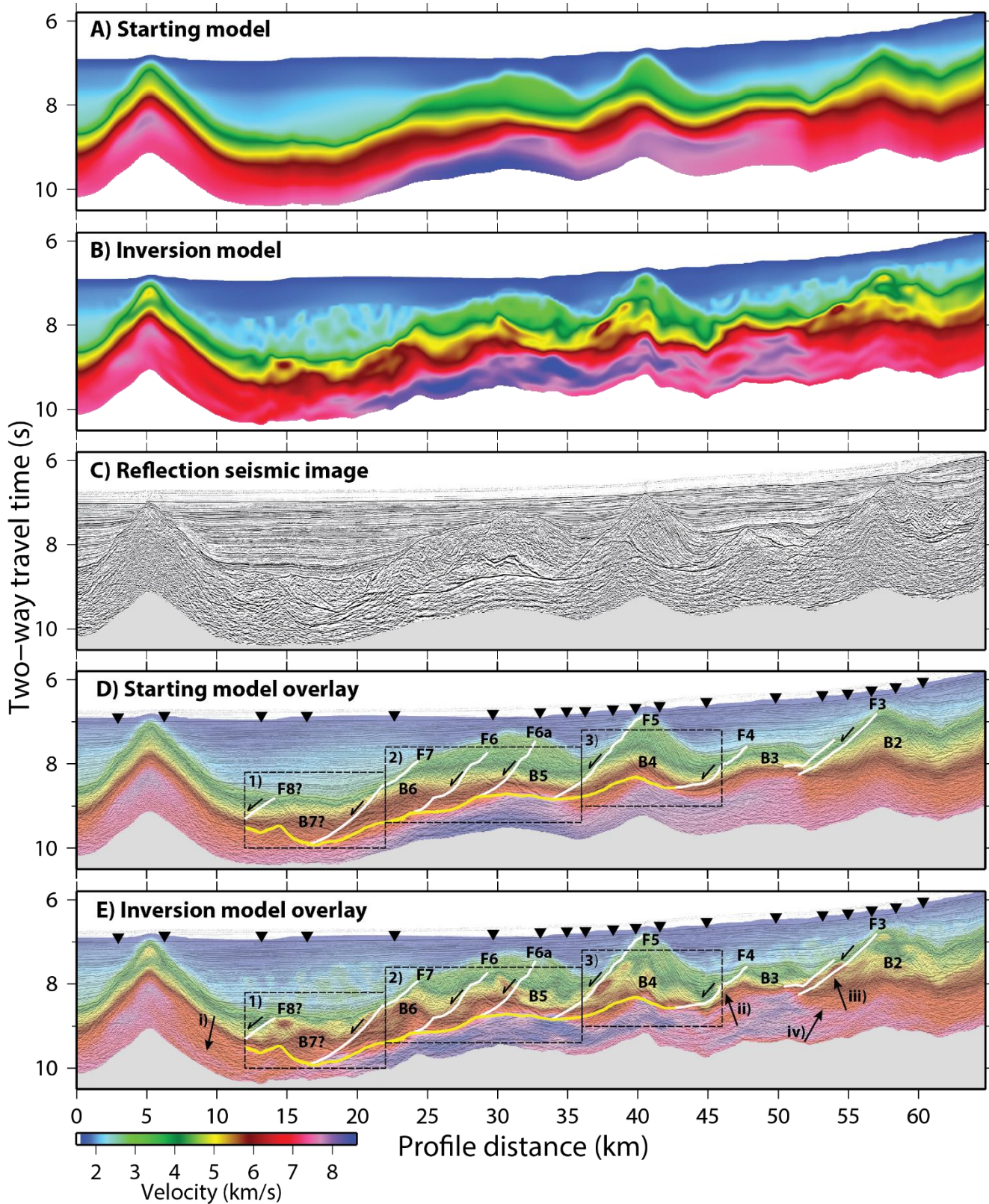
Figure 14: Comparison of large scale features with seismic reflection imaging. A) Starting velocity model B) Final FWI velocity model C) Kirchhoff pre-stack time-migrated multichannel seismic image of inline 420. D) Reflection image overlain with starting velocity model. E) Reflection image overlain with FWI velocity model. White lines indicate the location of interpreted normal faulting; the yellow line is the interpreted S reflector. Black upturned

957   triangles indicate the locations of utilised instruments. Dashed black rectangles indicate the

958   zoomed regions illustrated in Figure 4-15. Black arrows indicate regions discussed in the text.

959

960

961

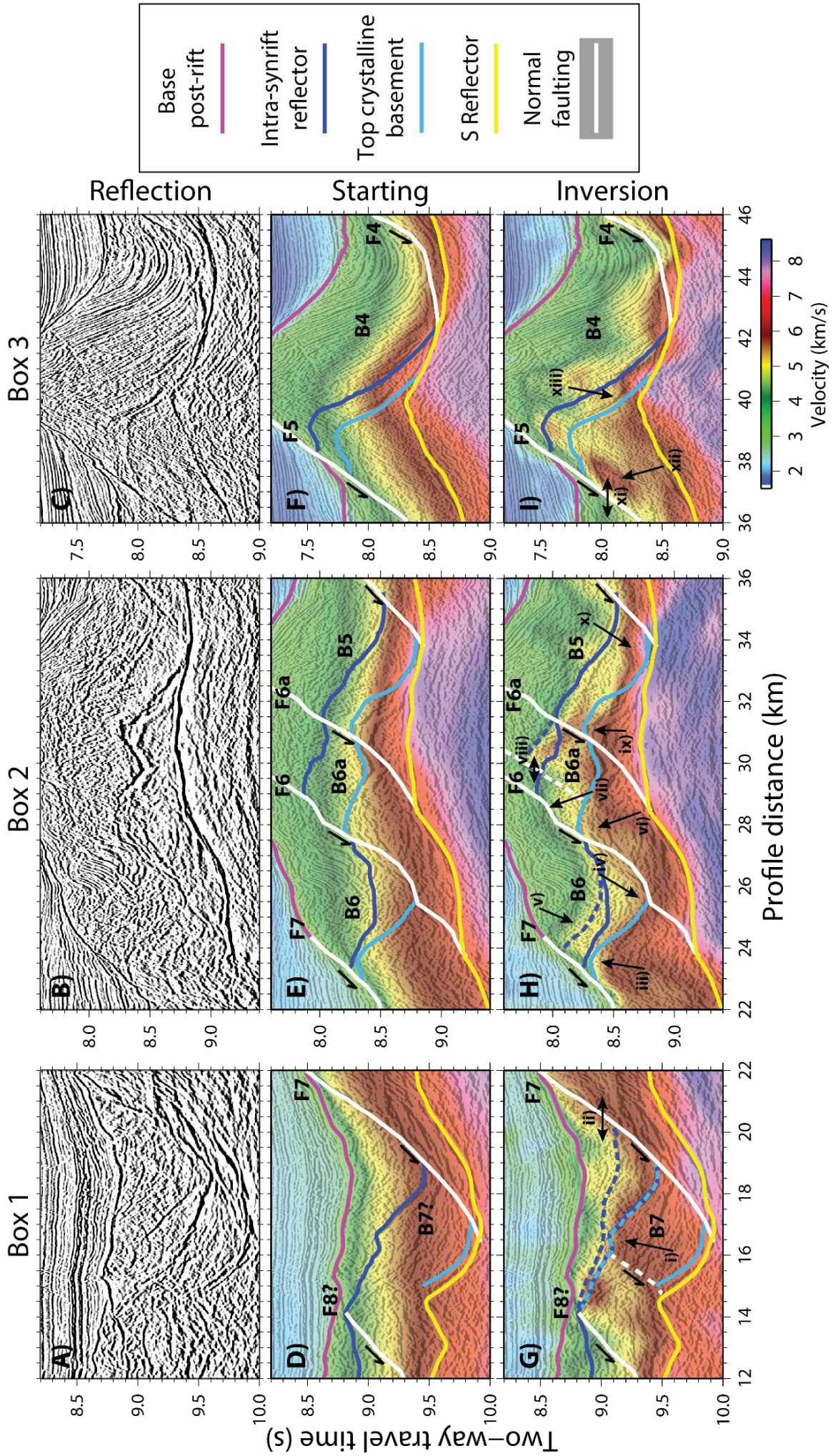962

963

964

965

966

967

968

969

Figure 15: Caption on next page.

Figure 15: A-C) Sections of interest of the Kirchhoff pre-stack time-migrated multichannel seismic image of inline 420. D-C) Same reflection images as A-C, overlain by the time-converted starting velocity model. G-I) Same reflection images as A-C, overlain by the time-converted final FWI velocity model. Interpreted faults and horizons: white lines indicate normal faulting; yellow lines indicate the S-reflector; pink line indicate the base of the post-rift sediments; dark blue indicate an intra syn-rift horizon; light blue indicates the top of crystalline basement. Black arrows indicate regions discussed in the text. Dashed lines indicate the reinterpretation of faults and horizons, based on the final FWI velocity model.
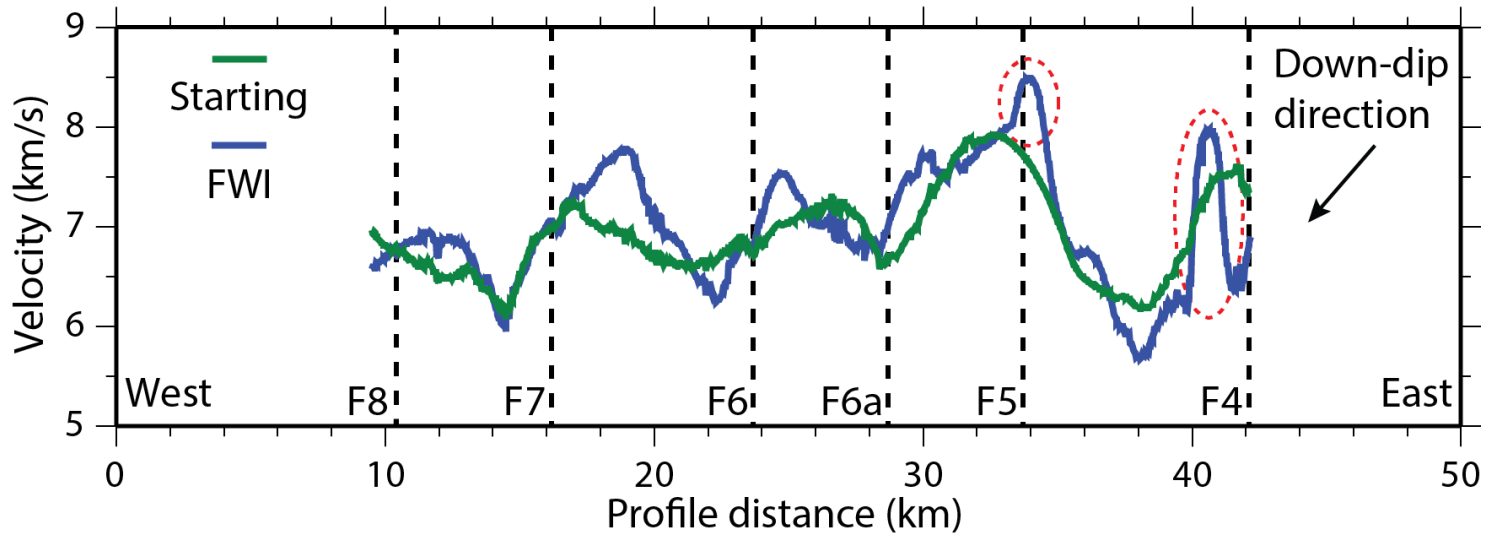
51

Figure 16: Velocities below the interpreted S-reflector (averaged over a 100 ms window). The green line indicates velocities from the starting velocity model; the blue line indicates velocities from the final FWI velocity model. Vertical dashed lines indicate the locations where interpreted normal faults sole onto the S-reflector. Red dashed ellipses indicate anomalous features of the inversion model.